# Spectroscopic Investigations of the Structural Phase Transition in Gd$_2$(Ti$_{1−y}$Zr$_y$)$_2$O$_7$ Pyrochlores

**N. J. Hess,\*,† B. D. Begg,‡ S. D. Conradson,§ D. E. McCready,† P. L. Gassman,† and W. J. Weber†**

*Pacific Northwest National Laboratory, PO Box 999, Richland, Washington 99352, ANSTO, PMB1, Menai, New South Wales 2234, Australia, and Los Alamos National Laboratory, Los Alamos, New Mexico 88545*

The Gd$_2$(Ti$_{1−y}$Zr$_y$)$_2$O$_7$ pyrochlore series undergoes a structural phase transition from pyrochlore ($Fd\bar{3}m$) to defect fluorite ($Fm\bar{3}m$) that can be driven compositionally by increasing the Zr content or thermally by sintering Zr-rich compositions at temperatures above 1550 °C. Our results demonstrate that ion-beam irradiation can also drive the structural phase transition for Zr-rich compositions. In an effort to understand the effects of composition and ion-beam irradiation on this phase transition, powder X-ray diffraction, polarized Raman, reflection infrared, and X-ray absorption spectroscopy experiments were conducted on Gd$_2$(Ti$_{1−y}$Zr$_y$)$_2$O$_7$ pyrochlores prior to and following irradiation with 2 MeV Au$^{2+}$ ions to a fluence of 5 ions/nm$^2$. Analysis of the vibrational and X-ray absorption data suggests that the structural integrity of the pyrochlore structure is based on distorted corner-shared TiO$_6$ or ZrO$_6$ octahedra. The vibrational spectra indicate that both anion and cation disorder precede the compositionally driven phase transition, but cation disorder appears to dominate the irradiation-driven transition. Analyses of the extended X-ray absorption fine structure of the Ti and Zr K edges and the Gd L$_{III}$ edges reveal a significant change in the Gd local environment upon irradiation and with increasing Zr content. The Ti and Zr local environments are less affected by irradiation or compositional change but show evidence of increasing disorder that can be attributed to rotations about shared polyhedral edges and corners.

## Introduction

Pyrochlore is one of a number of candidate materials proposed for the immobilization of actinide-rich wastes[1] and has recently been selected as a key component in the synroc-based pyrochlore-rich ceramics for the immobilization of surplus Pu in the United States.[2] The pyrochlores under consideration typically exhibit A$_2$B$_2$O$_7$ stoichiometry with the eight-coordinate A site occupied by large radius, tri- and tetravalent actinides and neutron-absorbing lanthanides and the six-coordinate B site occupied by either Ti or Zr. Because actinide-bearing crystalline waste forms will experience extensive α-recoil radiation damage, it is important to understand the effect of radiation damage on the pyrochlore structure. Considerable work has been carried out in characterizing the irradiation-induced crystalline-to-amorphous transformation observed in titanate-based pyrochlores[3−6] and radiation damage in naturally occurring pyrochlore minerals containing U and Th.[7] More recently, pyrochlores of Gd$_2$(Ti$_{1−y}$Zr$_y$)$_2$O$_7$ stoichiometry have been investigated that display a systematic decrease in susceptibility to radiation-induced amorphization with increasing Zr content commensurate with a phase transition from the pyrochlore structure to the defect fluorite structure. [8−10]

The ordered pyrochlore with A$_2$B$_2$X$_6$Y$_1$ stoichiometry belongs to the $Fd\bar{3}m$ space group and is a superstructure of the ideal defect fluorite structure ($Fm\bar{3}m$ space group) with exactly twice the lattice constant. The A and B cations occupy the 16c and 16d sites, respectively, with .$\bar{3}m$ symmetry. The X anions occupy the 48f site with 2.*mm* symmetry, and the Y anions occupy the 8a site with $\bar{4}3m$ symmetry. A symmetrically identical anion site, 8b, is systematically vacant. The structural phase transition from the $Fd\bar{3}m$ pyrochlore structure to the $Fm\bar{3}m$ ideal defect fluorite structure involves the randomization of the anions among the 48f, 8a, and 8b sites and the cations between the 16c and 16d sites. The equivalent anion and cations sites in the ideal defect fluorite structure are 8c ($\bar{4}3m$ symmetry) with 0.875 occupancy and 4a ($m\bar{3}m$ symmetry), respectively. Because short-range ordering of the A and B cations and anion vacancies almost always occurs, the ideal defect fluorite structure is never attained. The 48f site in the pyrochlore structure is slightly displaced from its corresponding position in the defect fluorite structure. The magnitude of displacement is specified by the value of the X anion positional parameter, $x_{48f}$. At its minimum value, 0.375, there is no displacement. At its maximum value, 0.4375, the 48f site is displaced toward the vacant 8b site. The phase transition between pyrochlore and defect fluorite structure is driven by the coupled anion occupancy of the 8b site, which results in a seventh oxygen atom coordinating the B cation, and the creation of an anion vacancy on the 8a site, which reduces the number of oxygen atoms coordinating the A cation.

Moon[11] proposed a scenario for the pyrochlore-to-fluorite transition in the Gd$_2$(Ti$_{1−y}$Zr$_y$)$_2$O$_7$ series on the basis of differences in ion mobility. Because the anions are more mobile than the cations, Moon argues that the observed anion disorder will always be in equilibrium with the cation disorder and that cation disorder is determined by thermal history. The degree of cation disorder is thought to be related to the ratio of the A

\* Corresponding author. E-mail: nancy.hess@pnl.gov.
† Pacific Northwest National Laboratory.
‡ ANSTO.
§ Los Alamos National Laboratory.

and B cationic radii.[12,13] As the ratio of the ionic radii approaches unity, the cation disorder increases, and hence the stability of the fluorite structure increases. Moon has demonstrated a relationship between the cation disorder parameter, $\Phi_c$, and the ionic radii ratio, $r_A/r_B$, that was consistent for both $Gd_2(Ti_{1-y}Zr_y)_2O_7$ and $Y_2(Ti_{1-y}Zr_y)_2O_7$ series pyrochlores.[11] However, Heremans et al.[14] followed the phase transition in the $Y_2(Ti_{1-y}Zr_y)_2O_7$ series using neutron diffraction, which is a sensitive probe of oxygen atom occupancy, and observed that anion disorder precedes cation disorder. The onset of anion disorder is marked by anions filling the vacant 8b anion site first with anions from the next nearest neighbor 48f site then by anions from the 8a site. The onset of cation disorder occurs upon creation of anion vacancies on the 8a site. At that stage, A and B cations disorder between the 16c and 16d sites.

Several studies of order−disorder transitions in pyrochlore have utilized Raman and infrared spectroscopy.[15−18] Vibrational spectroscopy has also been used to study self-radiation damage of naturally occurring actinide-bearing minerals[19−23] and ion-beam irradiated materials proposed for nuclear waste forms.[3,6,10,24] Vibrational spectroscopy is ideally suited to the study of crystalline-to-amorphous transitions because unlike diffraction-based techniques there is no requirement for lattice periodicity. In the analysis of cubic phases such as pyrochlore and fluorite, the vibrational selection rules require that the Raman-active and infrared-active vibrational modes be mutually exclusive. In studies of radiation-damaged materials, analysis of the Raman-active vibrational modes typically reveals a decrease in Raman intensity and broadening of the full width at half-maximum (fwhm) intensity of the Raman modes with increasing radiation-induced damage.[19−22] Most studies also report a minor decrease in the Raman vibrational frequency with increasing dose.[19−22,24] An infrared study on metamict minerals noted a loss of vibrational features with radiation damage.[23]

Extended X-ray absorption fine structure (EXAFS) spectroscopy has frequently been used to study the α-decay damage of natural minerals containing actinides[23,25−27] as well as Pu-substituted minerals[10,28−29] that have been proposed as actinide-containing phases in crystalline ceramic waste forms. Typically, such studies report similar changes in the EXAFS with increasing radiation damage: a decrease in the number of coordinating atoms in the first coordination sphere and minor changes in bond lengths. Accompanying these changes is a marked decrease in the amplitude of the second coordination sphere that has been interpreted as a loss in periodicity. Similarly, analysis of the X-ray absorption near edge structure (XANES) has also provided insights into the effects of radiation-induced disorder. However, quantitative analysis of the XANES is less well developed than the analysis of the EXAFS, so the interpretations of the changes observed in the XANES have been more limited. In this study, we have obtained EXAFS and XANES data on the Gd, Zr, and Ti cation sites to provide a detailed description of the cation environments in the $Gd_2(Ti_{1-y}Zr_y)_2O_7$ series pyrochlore as a function of compositional change and the result of ion-beam irradiation.

## Experimental Section

All samples were prepared via an alkoxide route from a liquid mixture of titanium isopropoxide, tetrabutyl zirconate, and gadolinium nitrate. These solutions were stir-dried and calcined at 700 °C for 1 h in air. The calcine was dried, ball-milled, and wet ball-milled before being pressed into pellets and sintered at 1600 °C for 50 h in air. The sintered pellets were polished to a 0.5-$\mu$m diamond finish and irradiated at room temperature

with 2 MeV $Au^{2+}$ ions to a fluence of 5 ions/nm² using the accelerator facilities within the Environmental Molecular Sciences Laboratory at Pacific Northwest National Laboratory.[30] In the case of the $Gd_2Ti_2O_7$ composition, it has been shown that a fluence of 5 ions/nm² is sufficient to obtain the amorphous state to a depth of 380 nm.[31]

X-ray diffraction (XRD) was carried out on a Philips PW3040/00 X'Pert MPD diffractometer using Cu Kα radiation. Approximately 0.5 g of the sintered pyrochlore pellets were mortar-ground to less than 325 mesh and loaded into an 18-mm diameter by 0.5-mm deep cell for X-ray analysis. Diffraction was collected from 10 to 80° ($2\theta$) at a rate of 0.02°/15 s. The analysis program RIQAS version 3.1 was used for Rietveld analysis. In addition, the lattice parameter, $a$, was refined using the software program Jade. The details of the glancing angle XRD studies on the irradiated samples have been reported elsewhere.[31]

Reflectance measurements were made in the mid- (MIR) and far-infrared (FIR) using a fixed-angle (30°) specular reflectance accessory. Analyses were made using the smallest aperture (4.8 mm) available for the reflectance accessory and the largest source aperture (12 mm). The moving mirror velocities were the same for both MIR and FIR (3 kHz). The infrared spectra were collected under vacuum using a Bruker IFS66v/S spectrophotometer. MIR spectra were obtained using a glowbar source, a KBr beam splitter, and a DLATGS detector equipped with a KBr window. The FIR spectra were obtained using a glowbar source with a 6-$\mu$m Mylar beam splitter and a DTGS detector. The actual measurement ranges were from 900 to 400 cm⁻¹ in the MIR and 550 to 50 cm⁻¹ in the FIR. All spectra were collected at 4 cm⁻¹ resolution and were divided by the background spectrum using a mirror placed at the knife edge. The resultant reflectance spectra from MIR and FIR were merged using an algorithm supplied by Bruker Optics. Both MIR and FIR spectra for each sample were obtained by averaging five sequentially collected spectra.

Polarized Raman spectra were measured in a backscattering geometry with a 1-mm spot size using approximately 500 mW of 488.0-nm excitation from a CW argon ion laser. The polarization of the Raman scattered light was scrambled prior to being focused on the entrance slit of a SPEX triple spectrometer. The exit slit was maintained at 75 $\mu$m, and the scattered light was then dispersed onto a liquid nitrogen-cooled charge-coupled device Ge detector. The detector was calibrated using the Raman lines of a $TiO_2$ (anatase) standard. The Raman signal was collected for 60 s for all samples. The Raman spectra were analyzed using the software package GRAMS/32. Vibrational-mode assignments were based on those found in the literature[10,32−33] as well as the results from normal-mode analysis using the software package VIBRAT.[34]

The XAS data were collected under dedicated operating conditions (3.0 GeV and 40−90 mA of current) using synchrotron radiation on beamlines 4−2 and 4−1 at the Stanford Synchrotron Radiation Laboratory. All spectra were collected at room temperature. Spectra were collected at the Ti and Zr K edge and the Gd $L_{III}$ edge in the fluorescence mode using a multielement germanium detector. Energy calibrations for the Ti and Zr edges were made by assigning the first inflection point in the absorption edges of Ti and Zr calibration foils to 4965.0 and 17 999.35 eV, respectively. The energy calibration for the Gd edges was made "internally" by assigning the first inflection point in the observed absorption spectra to 7245.0 eV. The absorption spectrum was normalized by fitting polynomials through the pre- and post-edge regions. At $E_0$, the

**TABLE 1: Powder X-ray Diffraction Results**

Rietveld and Lattice Parameter Refinements

| composition | lattice parameter, $a$ (Å) | $x_{48f}/R_p$ | literature values, $a$ (Å)/$x_{48f}$ |
|---|---|---|---|
| Gd$_2$Ti$_2$O$_7$ ($y = 0$) | 10.19278(8) | 0.4291(6)/5.47 | 10.185(1)/0.4263(34)[32] |
| Gd$_2$Ti$_{1.5}$Zr$_{0.5}$O$_7$ ($y = 0.25$) | | | |
| Gd$_2$Ti$_1$Zr$_1$O$_7$ ($y = 0.5$) | 10.3772(1) | 0.4219(7)/5.76 | |
| Gd$_2$Ti$_{0.5}$Zr$_{1.5}$O$_7$ ($y = 0.75$) | 10.4594(1) | 0.4152(6)/4.99 | |
| Gd$_2$Zr$_2$O$_7$ ($y = 1.0$) | 5.264$^a$ | | 10.523(0)/0.4089(9)$^{b,42}$ |

X-ray Determination of Structure Using Glancing Angle Techniques[31]

| composition | prior to irradiation | following irradiation |
|---|---|---|
| Gd$_2$Ti$_2$O$_7$ ($y = 0$) | pyrochlore | amorphous surface layer |
| Gd$_2$Ti$_{1.5}$Zr$_{0.5}$O$_7$ ($y = 0.25$) | pyrochlore | amorphous surface layer |
| Gd$_2$Ti$_1$Zr$_1$O$_7$ ($y = 0.5$) | pyrochlore | defect fluorite surface layer with buried amorphous layer |
| Gd$_2$Ti$_{0.5}$Zr$_{1.5}$O$_7$ ($y = 0.75$) | pyrochlore | defect fluorite |
| Gd$_2$Zr$_2$O$_7$ ($y = 1.0$) | defect fluorite with minor pyrochlore | defect fluorite |

$^a$ Defect fluorite structure. $^b$ Pyrochlore structure.

ionization threshold energy, the value of the extrapolated pre-edge was set to zero, and the difference between the extrapolations of the pre- and post-edge polynomials was set to unity. The energy scale of the data was converted from eV to $k$ space using the relationship $k = [(2m_e(E - E_0)/\hbar^2]^{1/2}$, where $m_e$ is the electron rest mass and $E_0$ values for the Ti, Zr, and Gd edges are set to 4982.8, 18614.7, and 7245.04 eV, respectively.

The XANES spectra consist of the normalized, background-subtracted absorption spectra extending from the pre-edge region to approximately 40 eV above the ionization threshold energy. The interpretation of the XANES profiles is usually limited to qualitative comparison to other samples in the Gd$_2$(Ti$_{1-y}$Zr$_y$)$_2$O$_7$ series or to standard compounds if available. However, recent theoretical developments[35−37] now permit extensive modeling of the experimental XANES and extraction of metric parameters that are complimentary to the analysis of the EXAFS data. Such studies have demonstrated that the XANES profiles are strongly dependent on the nearest-neighbor environment.[35,38]

The EXAFS oscillations were extracted by fitting a polynomial spline function through the post-edge region and normalizing the difference between this approximation of the solitary-atom EXAFS and the actual data with the absorption decrease calculated using the McMaster tables.[39] The number and position of the nodes in the spline were varied to minimize the integrated intensity in the Fourier transform moduli of the EXAFS between 0 and 1.8 Å. The resulting EXAFS oscillations are defined as $\chi(k) = [\mu(k) - \mu_{0,\text{spline}}(k)]/[\Delta\mu_{k=0}\mu_{0,M}(k)]$, where $\mu(k)$ is the observed absorption coefficient, $\mu_{0,\text{spline}}(k)$ is the fitted spline, $\Delta\mu_{k=0}$ is the observed absorption difference between the fitted spline and the extrapolation of the pre-edge polynomial at $k = 0$, and $\mu_{0,M}(k)$ is the calculated atomic absorption using the McMaster tables.[39] Fourier transforms were taken over photoelectron wavevector ranges that varied on the basis of the signal-to-noise ratio for each element. EXAFS nodes were selected as endpoints of the Fourier transform range, and a sine window function was used to dampen the EXAFS oscillations at the endpoints.

The phases and amplitudes for the interatomic scattering paths were calculated using the ab initio code FEFF7.02.[40,41] The normalized phases and amplitudes of the scattering paths were used to fit the experimentally measured EXAFS. Literature data for the Gd$_2$Ti$_2$O$_7$ [32] and Gd$_2$Zr$_2$O$_7$[42] structures were used to approximate the metal environment in pyrochlore. The number of atoms and the bond distances were determined using the normalized backscattering amplitude and phase functions from FEFF to fit the experimental EXAFS data using the following

equation, which is summed over all backscatters, $i$:

$$\chi(k) = \sum_i \frac{N_i S_i F_i(k)}{k R_i^2} \exp(-2k^2\sigma_i^2) \exp\left(\frac{-2R_i}{\lambda}\right) \sin(2kR_i + \phi_i(k))$$

$N_i$ is the number of backscattering atoms at a distance $R_i$ from the absorber. Values of the scale factor $S_i$ are typically determined empirically by fitting standards with calculated scattering amplitudes. Any necessary correction between the observed and calculated amplitude due to inelastic scattering not calculated by FEFF7.02[40,41] is then the assigned value of the scale factor $S_i$. This is not a very satisfactory approach because there are many experimental and sample-dependent artifacts that can affect the experimental amplitudes. In this work, we have chosen not to apply a correction factor to the FEFF calculated amplitudes; therefore, an $S_i$ value of 1 is used. The consequence of assigning $S_i$ a value of 1 is that the absolute number of atoms determined will be underestimated; however, the comparison of the number of atoms between related samples remains valid. The quantities $F_i(k) \exp(-2R_i/\lambda)$ and $f_i$ are the backscattering amplitude and phase functions, respectively, that are calculated by FEFF7.02 for each path. $\sigma_i^2$ is the Debye−Waller factor, and it represents the root-mean-squared variation in the absorber−backscatterer interatomic distance.

## Results

**X-ray Diffraction.** Insufficient quantities of Gd$_2$(Ti$_{1-y}$Zr$_y$)$_2$O$_7$ $y = 0.25$ material prevented the collection of diffraction data for Rietveld refinement of this composition. For the other samples, the refined lattice parameter, $a$, and the Rietveld refinement of the X anion positional parameter, $x_{48f}$, are given in Table 1. In general, there was good agreement between the Rietveld refinement and the observed diffractogram for the compositions analyzed. The refined values for the Ti endmember, Gd$_2$Ti$_2$O$_7$, of $a = 10.193$ Å and $x_{48f} = 0.4291$ are in good agreement with the data in the literature[32] ($a = 10.185$, $x_{48f} = 0.4263$). The compositional dependence of the X anion positional parameter, $x_{48f}$, is compared to that of the pyrochlore series Y$_2$(Ti$_{1-y}$Zr$_y$)$_2$O$_7$[14] in Figure 1. For a given Zr content, the X anion parameter for the Gd$_2$(Ti$_{1-y}$Zr$_y$)$_2$O$_7$ series has a larger value than for the Y$_2$(Ti$_{1-y}$Zr$_y$)$_2$O$_7$ series, which indicates a greater departure from the defect fluorite structure. A quadratic fit to the observed Y$_2$(Ti$_{1-y}$Zr$_y$)$_2$O$_7$ series dependence predicts
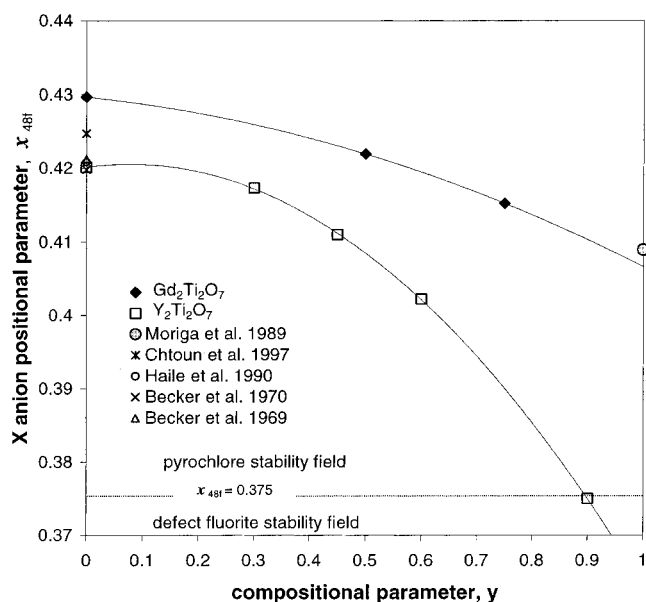
**Figure 1.** Comparison of the X anion fractional coordinate, $x_{48f}$, dependence on the compositional parameter, $y$, for the pyrochlore $Gd_2(Zr_yTi_{1-y})_2O_7$ series and the $Y_2(Zr_yTi_{1-y})_2O_7$ series measured by Heremans et al.[14] Literature values for the $Gd_2Zr_2O_7$ and $Y_2Ti_2O_7$ endmember compositions are also plotted (Moriga et al.,[42] Chtuon et al.,[45] Haile et al.,[46] Becker and White[47,48]). The pyrochlore and defect fluorite stability fields are delineated by the value of $x_{48f} = 0.375$ shown by the dotted line.

the Zr content, $y = 0.9$, at which the defect fluorite structure predominates, and this prediction has been confirmed experimentally.[14] The $Gd_2Zr_2O_7$ endmember ($y = 1.0$) of the $Gd_2(Ti_{1-y}Zr_y)_2O_7$ series in this study attained the defect fluorite structure as a result of synthesis conditions. However, literature data for the Zr endmember in the pyrochlore structure has a $x_{48f}$ value of 0.4089,[42] which is consistent with an extrapolation of the experimental measurements for the $y < 1.0$ compositions. The attainment of the defect fluorite structure for the $Gd_2Zr_2O_7$ composition is not unexpected, as it results from sintering at 1600 °C, which is above the order−disorder transition temperature of 1530 °C that defines the pyrochlore defect fluorite stability fields.[12]

Table 1 lists the phases identified by XRD for the pyrochlore series prior to and following irradiation. The surface of pyrochlores with compositions $0 \leq y \leq 0.5$ were rendered amorphous upon irradiation whereas the $y = 0.75$ pyrochlore underwent a phase transition from the pyrochlore to defect fluorite structure. The $y = 1.0$ sample retained the defect fluorite structure.

**Vibrational Spectroscopy.** Factor group analysis of $A_2B_2O_7$ pyrochlores in the $Fd\bar{3}m$ space group predicts the appearance of six Raman-active modes and seven infrared-active modes. Of the Raman-active modes, only the $A_{1g}$ mode should display significant changes in intensity with changes in polarization direction. Therefore, polarized Raman measurements permitted unequivocal identification of the vibrational frequency at 520 cm$^{-1}$ as the $A_{1g}$ mode, as shown in Figure 2. Note that the polarizability of the $A_{1g}$ mode decreases quickly as Zr replaces Ti on the B cation site and upon irradiation for a given composition. The second most intense Raman-active mode at 318 cm$^{-1}$ is assigned to the $E_g$ mode. There are three much weaker vibrational frequencies that are assigned to three of the four $T_{2g}$ modes. A broad peak at 680 cm$^{-1}$ may be the fourth $T_{2g}$ mode. Table 2 lists the observed Raman and infrared frequencies for the pyrochlore series prior to and following irradiation.
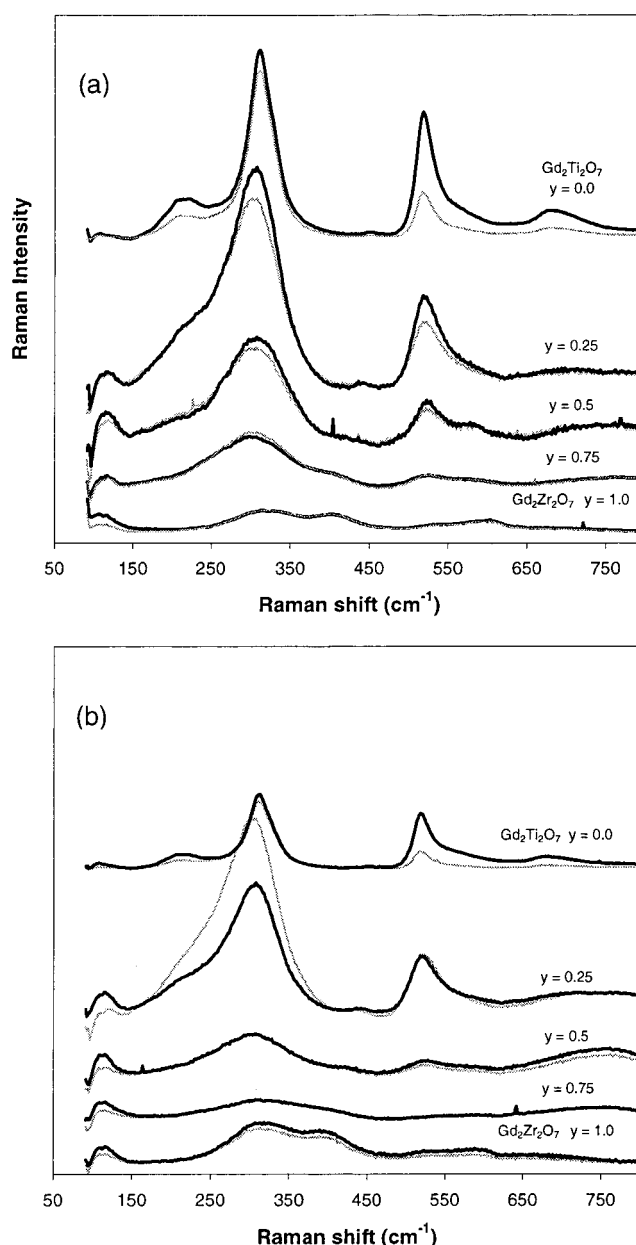




**Figure 2.** Polarized Raman spectra of the $Gd_2(Zr_yTi_{1-y})_2O_7$ pyrochlore series (a) prior to and (b) following irradiation. The dark trace represents the VV polarization, and the light trace is the VH polarization. The change in intensity of the mode at 520 cm$^{-1}$ with polarization direction identifies it as the $A_{1g}$ mode.

The Raman spectra of the pyrochlores show a marked change with Zr substitution on the B cation site. Namely, the $A_{1g}$ and $E_g$ modes disappear as would be expected from group theoretical considerations of the phase transition from the pyrochlore ($Fd\bar{3}m$) to defect fluorite ($Fm\bar{3}m$) structure. Group theory also specifies a reduction in the number of $T_{2g}$ modes commensurate with the phase transition from the $Fd\bar{3}m$ to $Fm\bar{3}m$ space group. Experimentally, systematic shifts in Raman frequencies are observed, and the fwhm intensities or line widths are unusually large for crystalline materials. Both thermal excitation of vibrational modes and static atomic displacement away from ideal positions can contribute to the fwhm of Raman-active modes. Static atomic displacement can be the result of lattice strain due to a sample's thermal history or compositional substitution by atoms with mismatched ionic radii or valence. The nearly linear increase of the fwhm of the $E_g$ mode with Zr substitution is compared to the work of Oueslati[13] in Figure 3.

Phase Transition in Gd$_2$(Ti$_{1-y}$Zr$_y$)$_2$O$_7$ Pyrochlores

*J. Phys. Chem. B, Vol. 106, No. 18, 2002* **4667**

**TABLE 2: Observed Raman and Infrared Frequencies**[a]

| prior to irradiation | | | | | | |
| --- | --- | --- | --- | --- | --- | --- |
| composition | $A_{1g}$ | $E_g$ | $T_{2g}$ | $T_{2g}$ | $T_{2g}$ | $T_{2g}$ |
| $y = 1.0$ (Gd$_2$Zr$_2$O$_7$) | 543 | 318 | | 597 | 407 | |
| $y = 0.75$ | 523 | 302 | | 575 | 404 | |
| $y = 0.5$ | 522 | 307 | | 572 | | 220 |
| $y = 0.25$ | 518 | 308 | | 547 | 441 | 235 |
| $y = 0.0$ (Gd$_2$Ti$_2$O$_7$) | 519 | 312 | | 549 | 455 | 219 |

| following irradiation | | | | | | |
| --- | --- | --- | --- | --- | --- | --- |
| composition | $A_{1g}$ | $E_g$ | $T_{2g}$ | $T_{2g}$ | $T_{2g}$ | $T_{2g}$ |
| $y = 1.0$ (Gd$_2$Zr$_2$O$_7$) | 535 | 315 | | 589 | 399 | |
| $y = 0.75$ | 550 | 318 | | 566 | 403 | |
| $y = 0.5$ | 522 | 308 | | 564 | | 258 |
| $y = 0.25$ | 519 | 308 | | 552 | 441 | 238 |
| $y = 0.0$ (Gd$_2$Ti$_2$O$_7$) | 518 | 312 | | 541 | 450 | 219 |

| prior to irradiation | | | | | | | |
| --- | --- | --- | --- | --- | --- | --- | --- |
| composition | $T_{1u}$ | $T_{1u}$ | $T_{1u}$ | $T_{1u}$ | $T_{1u}$ | $T_{1u}$ | $T_{1u}$ |
| $y = 1.0$ (Gd$_2$Zr$_2$O$_7$) | | 599 | 485 | 390 | 296 | 250 | 142 |
| $y = 0.75$ | | | 504 | | 306 | 256 | 142 |
| $y = 0.5$ | | | 509 | | 308 | 260 | 142 |
| $y = 0.25$ | | | 522 | 418 | 321 | 259 | 143 |
| $y = 0.0$ (Gd$_2$Ti$_2$O$_7$) | | | 530 | 433 | 329 | 264 | 145 |

| following irradiation | | | | | | | |
| --- | --- | --- | --- | --- | --- | --- | --- |
| composition | $T_{1u}$ | $T_{1u}$ | $T_{1u}$ | $T_{1u}$ | $T_{1u}$ | $T_{1u}$ | $T_{1u}$ |
| $y = 1.0$ (Gd$_2$Zr$_2$O$_7$) | | | | | | 233 | 142 |
| $y = 0.75$ | | | | | | 235 | 156, 136[b] |
| $y = 0.5$ | | | | | | 236 | 136 |
| $y = 0.25$ | | | | | | 236 | 137 |
| $y = 0.0$ (Gd$_2$Ti$_2$O$_7$) | | | | | 284 | 240 | 139 |

[a] All frequencies are in cm$^{-1}$. [b] Doublet peak.
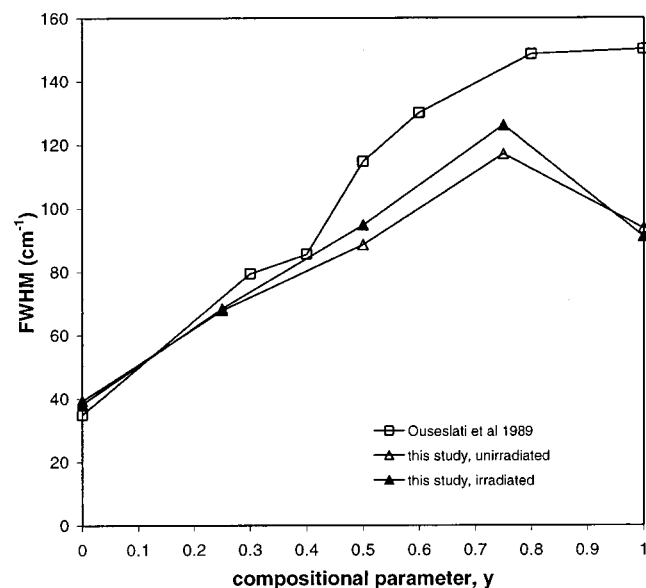


**Figure 3.** Comparison of the fwhm of the $E_g$ mode at 310 cm$^{-1}$ the for Gd$_2$(Zr$_y$Ti$_{1-y}$)$_2$O$_7$ pyrochlore series prior to and following irradiation in this study with the measurements from Oueslati et al.[41]

Similar values are observed for the $y = 0$, 0.25, and 0.5 compositions. However, with increasing Zr substitution, Oueslati observed increasingly broader line widths that may reflect increased lattice strain in these samples as a result of the differences in the heat treatment of the high Zr-containing samples. Specifically, following sintering at 1600 °C for 12 h, samples containing greater than 60% Zr were annealed at 1350 °C for 48 h to restore the pyrochlore structure.[13] As stated in the Experimental Section, the samples in this study were sintered

at 1600 °C for 50 h and were not followed by subsequent annealing below the pyrochlore-to-defect fluorite transition temperature. The defect fluorite-structured Zr endmember, Gd$_2$-Zr$_2$O$_7$, displays a decreased fwhm relative to the nearly linear trend displayed by the other compositions in this study. Upon irradiation, both broadening of the Raman lines and loss of Raman intensity are observed for the $0 < y < 0.75$ pyrochlores whereas no significant change is observed upon irradiation for the Zr endmember. Earlier Raman studies on ion-beam-irradiated Gd$_2$Ti$_2$O$_7$[6,24] showed a phase transition to the amorphous state. The lack of dramatic changes in the Raman spectra upon irradiation of the Ti-containing pyrochlores in this study is most likely the result of the laser probing beyond the ion-beam penetration depth ($\sim$300 nm). That is, the irradiation damage accumulates above the 300-nm depth, but the laser generating the Raman signal also samples the nonirradiated crystalline material below. Efforts were made to acquire the Raman spectra on thinned areas where the amount of nonirradiated crystalline material would be minimized; however, this approach was not effective.

As observed in the Raman spectra, the infrared spectra of the pyrochlore series shown in Figure 4(a) display a compositional dependence on the occupancy of the B cation. With increasing Zr substitution, fewer infrared absorption bands are observed. Spectra similar to the nonirradiated Gd$_2$Zr$_2$O$_7$ spectrum are observed upon irradiation for $0 < y < 0.5$ compositions (Figure 4b). For these samples, ion-beam irradiation appears to result in a disruption of the pyrochlore structure and the creation of a more fluorite-like structure. For $y > 0.75$ compositions, little change in the infrared spectra is observed following irradiation. All seven infrared-active modes have $T_{1u}$ symmetry. The decrease in the number of infrared absorption bands with increasing Zr content, as observed in the Raman spectra, is related to the phase transition from the pyrochlore to defect fluorite structure. For the infrared spectra, the symmetry of the infrared-active vibrational modes remains the same, but the number of modes is reduced from seven to three. Note that the infrared spectra collected in reflection geometry are more sensitive to the irradiation-driven structural changes than are the Raman spectra, which show relatively subtle spectral changes, because of the greater surface selectivity of the infrared spectroscopy in the reflection geometry.

Normal-mode analysis of the pyrochlore structure and the vibrational data was conducted using the software program Vibratz[34] assuming a simple valence model for the force constants. Six force constants, three linear and three bond angles, were defined to represent the vibrational structure of pyrochlore. The three linear force constants include one between Gd and each of the six oxygen atoms on the 48f site (Gd$-$O$_{48f}$), one between Gd and the two oxygen atoms on the 8a site (Gd$-$O$_{8a}$), and one between Ti or Zr atoms on the B cation site and the oxygen atoms on the 8a site (B$-$O$_{48f}$). The two intrapolyhedral angular force constants, O$-$Gd$-$O and O$-$Ti/Zr$-$O, and one interpolyhedral force constant, Gd$-$O$-$B, were defined for the Gd and B cations. Starting values for the force constants were taken from the vibrational study of the Pb$_2$Sc$_{0.5}$Ta$_{1.5}$O$_{6.5}$ pyrochlore.[43] The mass of the cation on the B site was adjusted appropriately to represent the changing composition of the sample upon Zr substitution. For example, for the Gd$_2$(Ti$_{1-y}$Zr$_y$)$_2$O$_7$ $y = 0.5$ pyrochlore, the mass of the B cation was the average of the Ti and Zr atomic masses. Using a linear regression routine, the values of the force constants were varied until the difference between the calculated and observed vibrational frequencies was minimized. Table 3 lists the
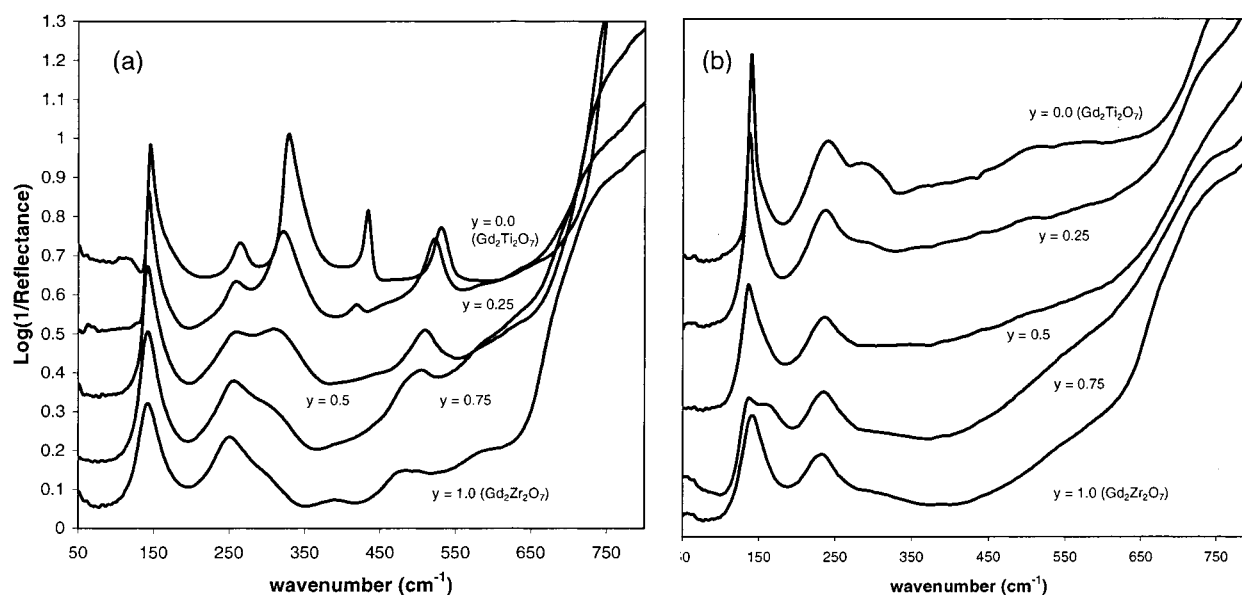
**Figure 4.** FTIR spectra of the $Gd_2(Zr_yTi_{1-y})_2O_7$ pyrochlore series (a) prior to and (b) following irradiation.

**TABLE 3: Initial and Regressed Force Constants (*md*/Å)**

| composition | Gd−O$_{48f}$ | Gd−O$_{8a}$ | B−O$_{48f}$ | O−Gd−O | O−B−O | Gd−O−B |
|---|---|---|---|---|---|---|
| initial values | 0.20 | 0.60 | 2.00 | 0.06 | 0.20 | 0.02 |
| $y = 1.0$ (Gd$_2$Zr$_2$O$_7$) | 0.0 | 0.47 | 1.02 | 0.37 | 0.15 | 0.11 |
| $y = 0.75$ | 0.0 | 0.51 | 1.14 | 0.30 | 0.17 | 0.03 |
| $y = 0.5$ | 0.0 | 0.52 | 0.93 | 0.30 | 0.17 | 0.0 |
| $y = 0.25$ | 0.0 | 0.50 | 1.00 | 0.29 | 0.17 | 0.0 |
| $y = 0.0$ (Gd$_2$Ti$_2$O$_7$) | 0.0 | 0.84 | 0.94 | 0.29 | 0.17 | 0.0 |

regressed force constants, and the regressed and the observed vibrational frequencies are listed in Table 1S, Supporting Information. An unexpected result is that for all compositions the linear force constant Gd−O$_{48f}$ regressed to zero, signifying the lack of a restoring force for displacements of the oxygen atoms toward or away from Gd. Note, however, that the linear force constant B−O$_{48f}$ between Ti or Zr and the same 48f oxygen atoms is the strongest force constant in the lattice, suggesting that these same oxygen atoms are tightly held at their equilibrium bond distance from the Ti or Zr atoms. Such a result supports earlier conclusions[12] that the pyrochlore structure is essentially maintained by strong BO$_6$ polyhedra. Normal-mode analysis was not attempted for the irradiated pyrochlore series because of indications that the Raman vibrational data collected for these samples were not purely representative of the radiation-damaged state.

In addition to calculating the frequency of vibration for each species, normal-mode analysis provides a description of the atomic displacements associated with each mode. The atomic motions associated with the $A_{1g}$ and $E_g$ Raman-active vibrational modes involve only the displacements of the oxygen atoms on the 48f site relative to other atoms in the unit cell. Interestingly, these displacements are directed toward the vacant 8b anion site. Raman-active $T_{2g}$ modes involve the displacements of oxygen atoms on both the 48f and 8a sites. The atomic displacements associated with the infrared-active modes involve both cation and anion displacements. In general, the lower infrared frequency modes have larger displacements of cations relative to those of anions. This description of the atomic displacements suggests that the Raman spectra should be sensitive to changes in the anionic sublattice whereas the low-frequency infrared spectra may reflect cation substitution

changes and cation disorder. Indeed, this is what is observed. The Raman spectra mainly exhibit changes in the polarizability, fwhm, and intensity of the active modes upon cationic substitutional changes, which may reflect the changes of the anionic sublattice. The infrared spectra exhibit significant spectral changes as a function of cationic compositional changes and upon irradiation, which likely reflect cation substitution and disorder of the cation sublattice due to irradiation.

**XAS Spectroscopy. XANES.** Gd L$_{III}$-edge XANES spectra of the pyrochlores prior to and following irradiation, shown in Figure 5, are dominated by the strong absorption peak or "white line" at 7250 eV, which results from the dipole-allowed 2p− 4d electronic transition. Prior to irradiation (Figure 5a), the XANES profiles are all quite similar and display isosbestic points, thus indicating that the compositional series is a function of only two Gd species and that their contributions are in accordance with the Beer−Lambert law for absorption.[44] Small variations in the intensity of the white line are also observed, but there is no systematic variation with composition. The appearance of the isosbestic points with Zr substitution on the B cation site implies that the Gd cation site can be represented by a mixture of two distinct Gd cation sites for all compositions. Upon irradiation (Figure 5b), the intensity of the white line increases for all compositions; however, no systematic variation with compositional change is discernible, and no isosbestic points are present.

Ti K-edge XANES spectra of the nonirradiated and irradiated pyrochlores are shown in Figure 6a and b, respectively. Subtle but systematic changes in the profile above the absorption edge are observed in the nonirradiated pyrochlores. However, the overall similarity of the XANES profiles suggests that the geometry of the Ti site remains stable despite increasing Zr
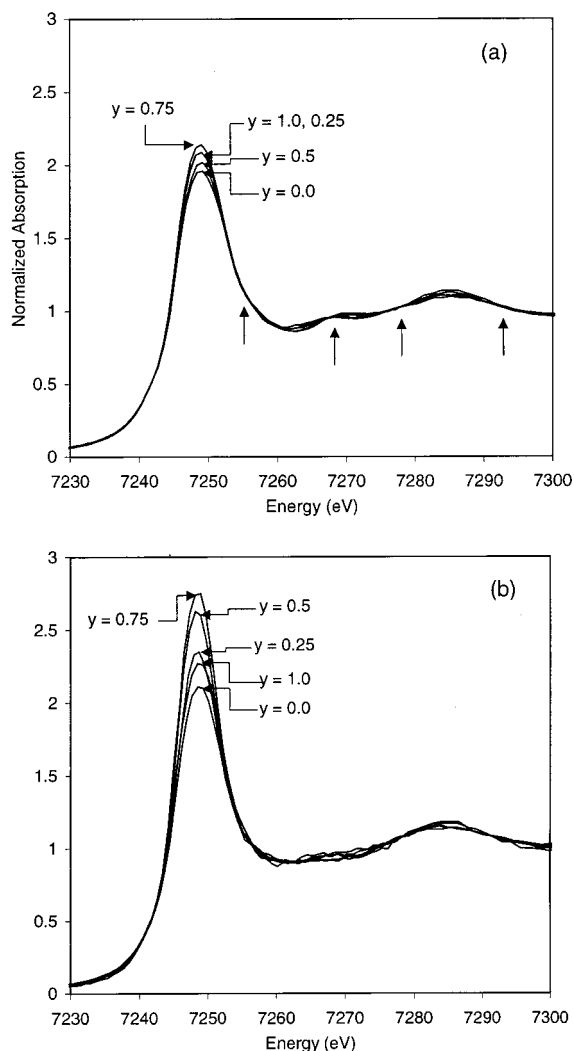
**Figure 5.** Gd L$_{\mathrm{III}}$-edge XANES for the Gd$_2$(Zr$_y$Ti$_{1-y}$)$_2$O$_7$ pyrochlore series (a) prior to and (b) following irradiation. The arrows in part (a) point to the isosbestic points mentioned in text.

substitution. Both the nonirradiated and irradiated pyrochlores display low-intensity pre-edge features at energies below the strong absorption peak at 4985 eV. Upon irradiation, the intensity of the pre-edge feature at 4970 eV increases for all compositions. An increase in intensity of this Ti pre-edge feature has been observed in previous radiation-damage studies of titanates.[22,25−26,28] This pre-edge feature has been assigned to a 1s−3d electronic transition that is dipole-forbidden but is allowed in the absence of centrosymmetric symmetry. The intensity of the pre-edge peak is a function of the d−p mixing that accompanies the distortion of the Ti cation site.[22] The increased intensity of the pre-edge peak upon irradiation indicates that the Ti site becomes distorted, thus allowing increased mixing of the atomic p orbitals of oxygen and the atomic d orbitals of titanium.

Zr K-edge XANES spectra of the pyrochlores prior to and following irradiation, shown in Figure 7a and b, respectively, display two well-defined peaks just above the absorption edge at 18 015 and 18 035 eV. Upon irradiation, there is a relative flattening of the second peak at 18 035 eV and the appearance of a weak pre-edge feature at approximately 18 005 eV. Unfortunately, because of the complexity of Zr K-edge XANES profiles and the lack of systematic changes with composition, it is not possible to draw conclusions regarding the significance of the observed changes.
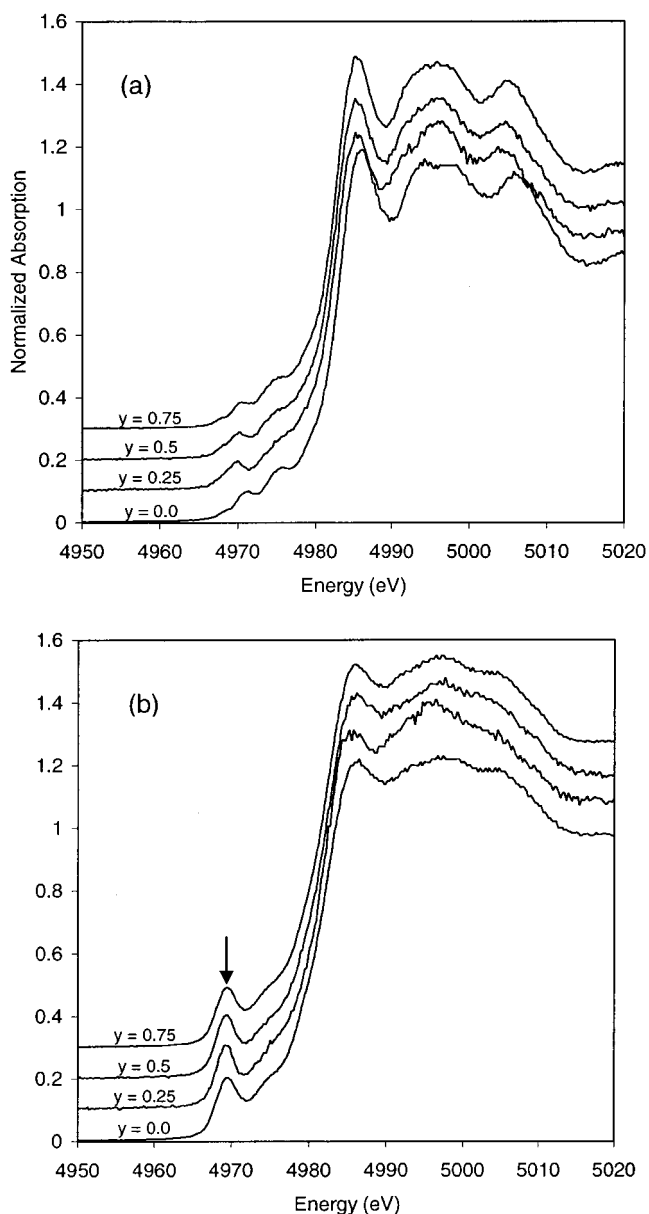


**Figure 6.** Ti K-edge XANES for the Gd$_2$(Zr$_y$Ti$_{1-y}$)$_2$O$_7$ pyrochlore series (a) prior to and (b) following irradiation. The irradiated samples in part (b) display a pre-edge feature indicated by an arrow.

**EXAFS.** Fourier transforms of the Gd L$_{\mathrm{III}}$-edge EXAFS contained contributions from backscattering atoms at radial distances greater than 6 Å. With such a large number of backscattering atoms, detailed analysis of the EXAFS becomes nonunique because of the high degree of correlation between parameters in eq 1. In particular, the parameter pairs $N_i$ and $\sigma_i^2$ and $R_i$ and $\delta E_{0,i}$ are highly correlated. For this reason, the Gd L$_{\mathrm{III}}$-edge EXAFS were filtered to remove the contributions at distances beyond 4.0 Å. The filtered Fourier transforms of the Gd L$_{\mathrm{III}}$-edge EXAFS for the Gd$_2$(Ti$_{1-y}$Zr$_y$)$_2$O$_7$ series pyrochlores are shown in Figure 8a and b for pyrochlores prior to and following irradiation, respectively. Prior to irradiation, there is a systematic change in the appearance of the transforms as Zr substitutes for Ti on the B cation site. Gd, in the Gd$_2$Ti$_2$O$_7$ pyrochlore ($y = 0$), has eight nearest-neighbor oxygen atoms distributed between two Gd−O distances that are separated by 0.25 Å. The contributions from these two oxygen shells interfere destructively, giving rise to the two low-intensity peaks at ∼2 Å. The intense peak at a radial distance of ∼3.3 Å corresponds to the next-nearest-neighbor shell consisting of Gd and Ti atoms
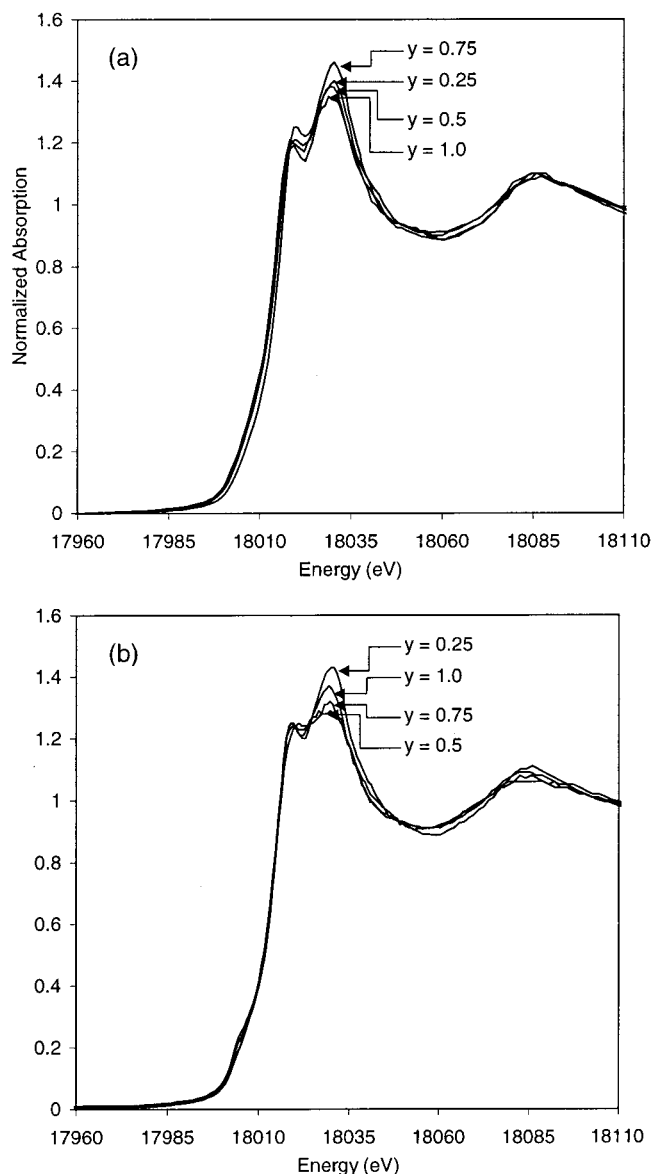
**Figure 7.** Zr K-edge XANES for the $Gd_2(Zr_yTi_{1-y})_2O_7$ pyrochlore series (a) prior to and (b) following irradiation.



**Figure 8.** Fourier transforms of the Gd $L_{III}$-edge EXAFS for the $Gd_2(Zr_yTi_{1-y})_2O_7$ pyrochlore series (a) prior to and (b) following irradiation.

on the A and B cation sites, respectively. Ideally, the Gd environment in the $Gd_2Zr_2O_7$ pyrochlore ($y = 1$, defect fluorite structure) consists of seven oxygen atoms at a single distance. Correspondingly, the increased intensity of the transform peak at $\sim2$ Å results from the constructive interference of the backscattering oxygen atoms at a single distance. The decrease in the intensity of the peak at $\sim3.3$ Å results from the destructive interference of the Gd−Gd and Gd−Zr backscattering contributions to the EXAFS that is due to differences in the phase and amplitude functions of Gd and Zr atoms at the same interatomic distance. Following irradiation, all compositions display an increase in the intensity of the Gd−O shell ($\sim2$ Å) and a decrease in the intensity of the shell consisting of Gd−Gd/Ti/Zr contributions ($\sim3.3$ Å).

The results of fits to the Gd $L_{III}$-edge EXAFS are given in Table 4. The interatomic distances determined from the EXAFS are in good agreement with those calculated from published X-ray diffraction results[32,42] and those determined for $y = 0.5$ and 0.75 compositions in this study, with the exception of the Gd−$O_{48f}$ distance, which is shorter than expected by 0.12 Å. In addition, the distribution of oxygen atoms between the
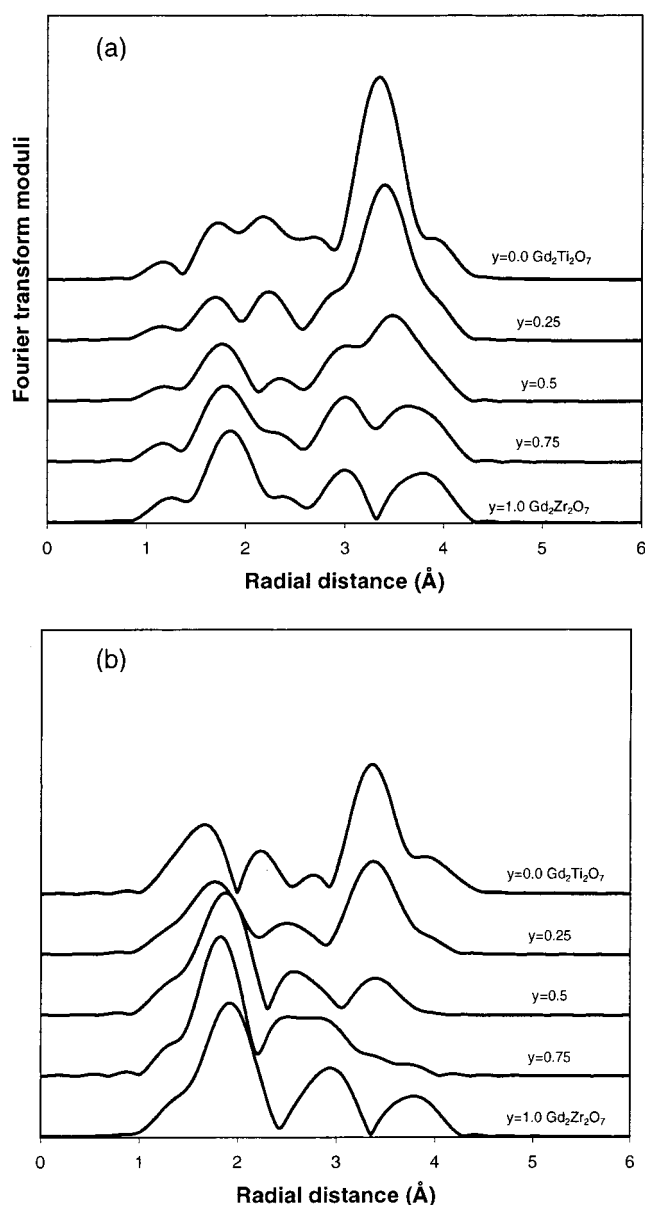
8a and 48f sites changes progressively with increasing Zr substitution for Ti on the B cation site. For the $y = 0$ composition ($Gd_2Ti_2O_7$), the oxygen atoms reside predominately on the more distant 48f site whereas for the $y = 1$ composition ($Gd_2Zr_2O_7$) the oxygen atoms are predominately on the closer 8a site. Because there are only two 8a sites available to coordinate Gd in the pyrochlore structure, the increase in the number of oxygen atoms at the shorter interatomic distance with increasing Zr substitution must represent a distortion of the Gd site to a geometry more similar to the defect fluorite structure rather than increased anion disorder. Fits to the next-nearest shell were more complicated because the substitution of Zr for Ti on the B cation site means that the next-nearest-neighbor shell (cation shell) is composed of Gd, Ti, and Zr atoms, each with their own phase and amplitude backscattering functions. The contributions to the total EXAFS interfere constructively or destructively depending on the sum of the individual phase and amplitude functions, the disorder associated with each cation, and minor differences in interatomic distances. Therefore, the fitting parameters associated with the cation shell were

**TABLE 4: Gd $L_{III}$-edge EXAFS Fitting Results for the A-site Cation, Gd, for the $Gd_2(Zr_yTi_{1-y})_2O_7$ Pyrochlore Series**

| | unirradiated[a] | | | | |
|---|---|---|---|---|---|
| sample | $y = 0$ | $y = 0.25$ | $y = 0.5$ | $y = 0.75$ | $y = 1.0$ |
| $Gd-O_{8a}$ | (2.21) | (2.23) | (2.25) | (2.26) | (2.28) |
| distance (Å) | $2.20 \pm 0.02$ | $2.26 \pm 0.02$ | $2.28 \pm 0.02$ | $2.28 \pm 0.02$ | $2.29 \pm 0.02$ |
| number | $2.5 \pm 0.5$ | $4.8 \pm 1.0$ | $4.5 \pm 0.8$ | $4.8 \pm 0.9$ | $5.4 \pm 1.1$ |
| $\sigma$ (Å) | $0.06 \pm 0.01$ | $0.13 \pm 0.01$ | $0.12 \pm 0.01$ | $0.10 \pm 0.01$ | $0.11 \pm 0.01$ |
| $Gd-O_{48f}$ | (2.57) | (2.57) | (2.56) | (2.53) | $(2.50/2.28)^b$ |
| distance (Å) | $2.45 \pm 0.02$ | $2.50 \pm 0.01$ | $2.51 \pm 0.01$ | $2.48 \pm 0.01$ | $2.51 \pm 0.02$ |
| number | $3.9 \pm 1.0$ | $1.7 \pm 0.4$ | $0.7 \pm 0.2$ | $0.6 \pm 0.2$ | $0.4 \pm 0.2$ |
| $\sigma$ (Å) | $0.09 \pm 0.01$ | $0.04 \pm 0.02$ | $0.01 \pm 0.00$ | $0.00 \pm 0.00$ | $0.01 \pm 0.00$ |
| $Gd-Gd$ | (3.60) | (3.64) | (3.67) | (3.70) | (3.72) |
| distance (Å) | $3.60 \pm 0.01$ | $3.64 \pm 0.01$ | $3.67 \pm 0.01$ | $3.69 \pm 0.01$ | $3.70 \pm 0.01$ |
| number | $5.7 \pm 1.2$ | 6, fixed | 6, fixed | 6, fixed | $5.7 \pm 1.2$ |
| $\sigma$ (Å) | $0.08 \pm 0.01$ | $0.07 \pm 0.01$ | $0.09 \pm 0.01$ | $0.09 \pm 0.01$ | $0.09 \pm 0.01$ |
| $Gd-Ti$ | (3.60) | (3.64) | (3.67) | (3.70) | (3.72) |
| distance (Å) | $3.64 \pm 0.02$ | $3.67 \pm 0.01$ | $3.66 \pm 0.01$ | $3.65 \pm 0.03$ | |
| number | $8.4 \pm 2.,0$ | 4.5, fixed | 3, fixed | 1.5, fixed | |
| $\sigma$ (Å) | $0.12 \pm 0.01$ | $0.09 \pm 0.01$ | $0.13 \pm 0.01$ | $0.14 \pm 0.01$ | |
| $Gd-Zr$ | | (3.64) | (3.67) | (3.70) | (3.72) |
| distance (Å) | | $3.66 \pm 0.01$ | $3.69 \pm 0.01$ | $3.69 \pm 0.01$ | $3.68 \pm 0.02$ |
| number | | 1.5, fixed | 3, fixed | 4.5, fixed | $7.5 \pm 1.9$ |
| $\sigma$ (Å) | | $0.00 \pm 0.00$ | $0.09 \pm 0.01$ | $0.10 \pm 0.01$ | $0.12 \pm 0.01$ |
| $R^2$ | 0.4555 | 0.2375 | 0.1725 | 0.2227 | 0.3192 |

| | irradiated | | | | |
|---|---|---|---|---|---|
| sample | $y = 0$ | $y = 0.25$ | $y = 0.5$ | $y = 0.75$ | $y = 1.0$ |
| $Gd-O_{8a}$ | | | | | |
| distance (Å) | $2.23 \pm 0.02$ | $2.28 \pm 0.02$ | $2.29 \pm 0.03$ | $2.28 \pm 0.03$ | $2.29 \pm 0.02$ |
| number | $3.8 \pm 0.8$ | $5.8 \pm 1.0$ | $5.7 \pm 1.3$ | $5.6 \pm 1.2$ | $5.3 \pm 1.1$ |
| $\sigma$ (Å) | $0.09 \pm 0.01$ | $0.12 \pm 0.01$ | $0.10 \pm 0.01$ | $0.08 \pm 0.01$ | $0.09 \pm 0.01$ |
| $Gd-O_{48f}$ | | | | | |
| distance (Å) | $2.45 \pm 0.01$ | $2.52 \pm 0.01$ | $2.61 \pm 0.02$ | $2.51 \pm 0.02$ | $2.36 \pm 0.02$ |
| number | $2.2 \pm 0.5$ | $0.8 \pm 0.2$ | $0.5 \pm 0.2$ | $0.8 \pm 0.2$ | $0.6 \pm 0.2$ |
| $\sigma$ (Å) | $0.05 \pm 0.01$ | $0.05 \pm 0.02$ | $0.00 \pm 0.00$ | $0.00 \pm 0.00$ | $0.00 \pm 0.00$ |
| $Gd-Gd$ | | | | | |
| distance (Å) | $3.61 \pm 0.01$ | $3.63 \pm 0.01$ | $3.60 \pm 0.02$ | $3.61 \pm 0.01$ | $3.68 \pm 0.01$ |
| number | $1.8 \pm 0.4$ | 6, fixed | 6, fixed | 6, fixed | $5.8 \pm 1.4$ |
| $\sigma$ (Å) | $0.03 \pm 0.02$ | $0.10 \pm 0.01$ | $0.11 \pm 0.02$ | $0.10 \pm 0.01$ | $0.09 \pm 0.01$ |
| $Gd-Ti$ | | | | | |
| distance (Å) | $3.64 \pm 0.02$ | $3.72 \pm 0.01$ | $3.72 \pm 0.02$ | $3.64 \pm 0.01$ | |
| number | $5.8 \pm 1.5$ | 4.5, fixed | 3, fixed | 1.5, fixed | |
| $\sigma$ (Å) | $0.13 \pm 0.01$ | $0.14 \pm 0.01$ | $0.10 \pm 0.01$ | $0.05 \pm 0.01$ | |
| $Gd-Zr$ | | | | | |
| distance (Å) | | $3.49 \pm 0.01$ | $3.59 \pm 0.01$ | $3.62 \pm 0.01$ | $3.67 \pm 0.01$ |
| number | | 1.5, fixed | 3, fixed | 4.5, fixed | $6.6 \pm 1.7$ |
| $\sigma$ (Å) | | $0.09 \pm 0.00$ | $0.13 \pm 0.01$ | $0.08 \pm 0.00$ | $0.11 \pm 0.01$ |
| $R^2$ | 0.3047 | 0.2147 | 0.4650 | 0.4874 | 0.4148 |

| | mixture of $Gd_2Ti_2O_7$ and $Gd_2Zr_2O_7$ $Gd-O$ environments | | | | |
|---|---|---|---|---|---|
| sample | $y = 0$ | $y = 0.25$ | $y = 0.5$ | $y = 0.75$ | $y = 1.0$ |
| $Gd_2Ti_2O_7$ | 0.99 | 0.79 | 0.39 | 0.26 | 0.14 |
| $Gd_2Zr_2O_7$ | 0.01 | 0.21 | 0.61 | 0.74 | 0.86 |
| $R^2$ | 0.4584 | 0.3751 | 0.2337 | 0.2693 | 0.3087 |

[a] The values in parentheses are calculated interatomic distances in Å from XRD determinations of the lattice parameter, $a$, and the X anion positional parameter, $x_{48f}$, given in Table 1. These values were interpolated for the $y = 0.25$ composition. [b] Based on the anion positional parameter $x_{48f} = 0.4089$ reported in the literature[42]. XRD results indicate that this sample is predominately defect fluorite structured with minor pyrochlore content

constrained by fixing the number of Gd, Ti, and Zr atoms at the stoichiometric composition appropriate for each sample. Even given this constraint, the fitting results for the cation shell are not robust. Nevertheless, a reasonable fit is obtained that is in good agreement with the X-ray diffraction data. The Gd−Gd and Gd−Zr interatomic distances increase with increasing Zr substitution, as predicted from the increase in the lattice parameter with changing composition. However, the Gd−Ti interatomic distance appears to remain relatively constant over the entire pyrochlore series.

Given that the presence of isosbestic points in the Gd $L_{III}$-edge XANES spectra suggest that the Gd−O environment

throughout the pyrochlore series can be described as a binary mixture of distinct $Gd_2Ti_2O_7$ and $Gd_2Zr_2O_7$ endmember environments, the EXAFS spectra were also fit using an alternative approach based on this suggestion. The filtered Gd $L_{III}$-edge EXAFS were fit using a Gd−O environment representative of $Gd_2Ti_2O_7$ and $Gd_2Zr_2O_7$ as determined from fits to the EXAFS of the $y = 0$ and $y = 1.0$ compositions, namely, 2.5 oxygen atoms at 2.20 Å with 4 oxygen atoms at 2.45 Å for $Gd_2Ti_2O_7$ and 4.5 oxygen atoms at 2.29 Å for $Gd_2Zr_2O_7$. In this series of fits, only the proportional contribution of these two environments was allowed to change; all other parameters including interatomic distance, number of atoms, $\sigma$, and $dE_0$ were fixed.

Because of the large separation in interatomic distance between the Gd−O shell and the more distant shells, no attempt was made to restrain the more distant shells. Even so, no significant changes in the fitting results for these distant shells were observed in the new fits relative to those presented in Table 4. The quality of the fit, $R^2$, yielded by this approach is quite comparable to the results obtained by determining the average Gd−O environment and indicated a progressive change from an essentially pure $Gd_2Ti_2O_7$ -like Gd−O environment for the $y = 0$ composition to one consisting of an 86% $Gd_2Zr_2O_7$ and a 14% $Gd_2Ti_2O_7$ -like Gd−O environment for the $y = 1$ composition. The results of this fitting approach are summarized in Table 4 and allow two conclusions to be drawn. First, changes in the Gd−O environment as a function of composition can be represented by a proportional mixture of the $Gd_2Ti_2O_7$ and $Gd_2$-$Zr_2O_7$ Gd−O environments. Second, as Zr substitutes for Ti on the B site, the proportion of Gd−O environments gradually shifts from one endmember to the other. These results are consistent with the results of the traditional EXAFS fitting approach, but, moreover, they suggest the presence of localized and coexisting domains of pyrochlore and defect fluorite-like Gd coordination environments, the proportion of which changes as a function of composition across the pyrochlore series.

Following irradiation, the distribution of nearest-neighbor oxygen atoms changes such that the majority of oxygen atoms are at the shorter 2.28 Å interatomic distance for all compositions (Table 4). This 2.28 Å distance is consistent with a defect fluorite-structured Gd−O environment. The redistribution of oxygen atoms is also suggested by the radial distribution plots, shown in Figure 8b, that show an increase in the intensity of the Gd−O shell at ∼2 Å with irradiation. Although the validity of the fitting results for the Gd cation shell for the intermediate compositions is questionable, the lower intensity of the transform peaks at ∼3.3 Å suggests that cation disordering occurs upon irradiation. In addition, there appears to be a relative shortening of the Gd−Gd and Gd−Zr interatomic distances and a lengthening of the Gd−Ti interatomic distance whereas the Gd−Gd, Gd−Ti, and Gd−Zr interatomic distances were nearly equivalent prior to irradiation in all samples in the series.

The Fourier transforms of the Ti K-edge EXAFS for the $Gd_2(Ti_{1-y}Zr_y)_2O_7$ series pyrochlores are shown in Figure 9 prior to and following irradiation. The intense peaks at an ∼1.5 Å radial distance corresponds to the Ti−O shell, and the second intense peak at a radial distance of ∼3.3 Å corresponds to the cation shell composed of Gd and varying proportions of Zr and Ti. No systematic change in the appearance of the transforms is observed as Zr substitutes for Ti on the B site, suggesting that the B cation site in pyrochlore and the cation site in defect fluorite structures are quite similar. Small variations in the position of the Ti−O peak are observed with changing composition. Upon irradiation, the most significant changes are the decrease in intensity of the Ti−O peak (∼1.5 Å) and the near-disappearance of the Ti cation peak (∼3.3 Å).

The results of fits to the Ti K-edge EXAFS are given in Table 5. Although only one Ti−O distance is predicted by the structure, two oxygen shells were required to represent the Ti−O EXAFS. The interatomic distance of the shorter one, at approximately 1.94 Å, is in good agreement with the value determined by X-ray diffraction data for $Gd_2Ti_2O_7$ ($y = 0$). However, the agreement becomes less satisfactory with increasing Zr substitution. The fitted interatomic distance remains unchanged whereas the predicted interatomic distance, based on the lattice parameter and the value of the X anion positional parameter for each composition, increases. The longer Ti−O
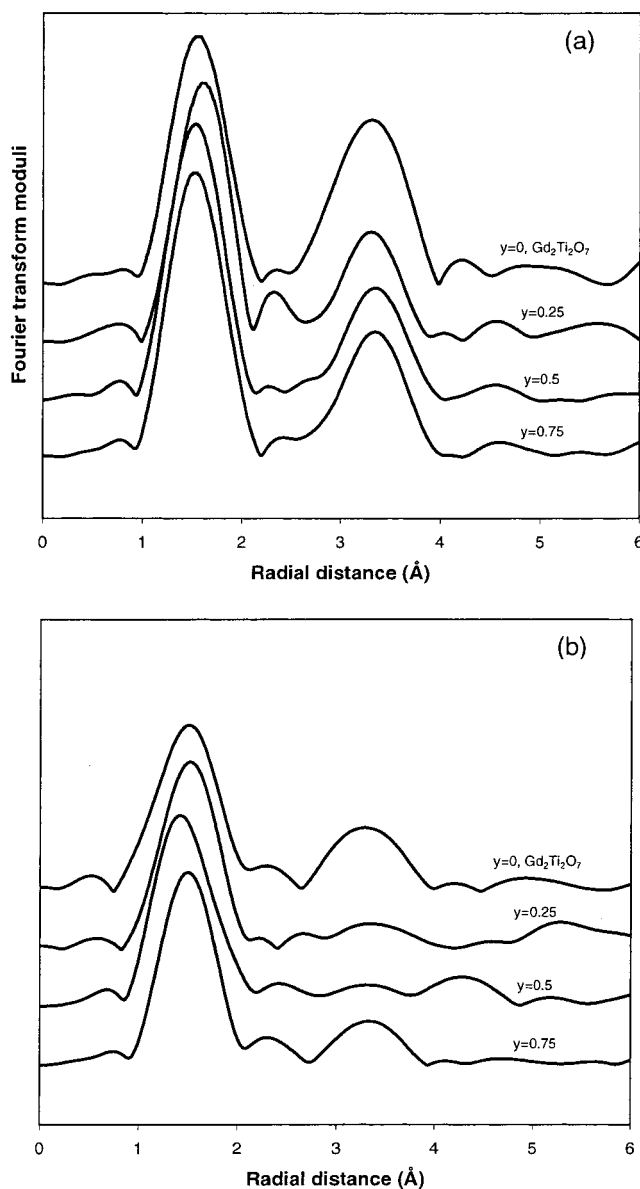


**Figure 9.** Fourier transforms of the Ti K-edge EXAFS for the $Gd_2(Zr_yTi_{1-y})_2O_7$ pyrochlore series (a) prior to and (b) following irradiation.

interatomic distance, at 2.06 Å, may correspond to oxygen atoms occupying the vacant 8b site. The longer Ti−O distance also fails to display a systematic dependence on composition but suggests that a degree of anion disordering occurs throughout the compositional range. Upon irradiation, there is a slight decrease in both Ti−O interatomic distances for all compositions and a slight decrease in the number of oxygen atoms coordinating Ti. Both of these changes may contribute to the decreased centrosymmetric symmetry that allows the dipole-forbidden pre-edge feature in the Ti K-edge XANES to increase in intensity upon irradiation. The fitting results for the cation shell composed of Gd, Ti, and Zr atoms suggest that the interatomic distances are ordered from shorter to longer in the sequence Ti−Gd < Ti−Ti < Ti−Zr. None of the interatomic distances show a compositional dependence. The decreased amplitude observed in the transforms of the Ti cation shell (∼3.3 Å) upon irradiation is reflected by an increase in σ. Because σ is a measure of the disorder or distribution of atoms about that interatomic distance, the increase in σ with irradiation suggests more disorder about those sites. In addition, a slight increase in the Ti−Ti interatomic distance is also observed upon irradiation.

Phase Transition in Gd$_2$(Ti$_{1-y}$Zr$_y$)$_2$O$_7$ Pyrochlores

*J. Phys. Chem. B, Vol. 106, No. 18, 2002* **4673**

**TABLE 5: Ti K-edge EXAFS Fitting Results for EXAFS Fitting Results for the Gd$_2$(Zr$_y$Ti$_{1-y}$)$_2$O$_7$ Pyrochlore Series**

| | unirradiated[a] | | | | |
|---|---|---|---|---|---|
| sample | $y = 0$ | $y = 0.25$ | $y = 0.5$ | $y = 0.75$ | $y = 1.0$ |
| Ti−O$_{48f}$ | (1.94) | (1.97) | (2.00) | (2.05) | |
| distance (Å) | 1.94 ± 0.02 | 1.96 ± 0.02 | 1.94 ± 0.01 | 1.95± 0.02 | |
| number | 4.0 ± 1.0 | 3.0 ± 0.8 | 4.4 ± 1.0 | 4.0 ± 1.2 | |
| σ (Å) | 0.00 ± 0.00 | 0.00 ± 0.00 | 0.00 ± 0.00 | 0.00 ± 0.00 | |
| Ti−O$_{8b}$ | | | | | |
| distance (Å) | 2.05 ± 0.02 | 2.06 ± 0.02 | 2.06 ± 0.02 | 2.07 ± 0.02 | |
| number | 2.8 ± 0.8 | 4.0 ± 1.2 | 3.4 ± 1.0 | 2.8 ± 0.8 | |
| σ (Å) | 0.00 ± 0.00 | 0.00 ± 0.00 | 0.00 ± 0.00 | 0.00 ± 0.00 | |
| Ti−Gd | (3.60) | (3.64) | (3.67) | (3.70) | |
| distance (Å) | 3.59 ± 0.01 | 3.57 ± 0.02 | 3.60 ± 0.02 | 3.59 ± 0.01 | |
| number | 6.4 ± 1.7 | 6, fixed | 6, fixed | 6, fixed | |
| σ (Å) | 0.08 ± 0.01 | 0.11 ± 0.01 | 0.11 ± 0.01 | 0.09 ± 0.01 | |
| Ti−Ti | (3.60) | (3.64) | (3.67) | (3.70) | |
| distance (Å) | 3.66 ± 0.01 | 3.63 ± 0.02 | 3.65 ± 0.01 | 3.65 ± 0.01 | |
| number | 5.6 ± 1.5 | 4.5, fixed | 3, fixed | 1.5, fixed | |
| σ (Å) | 0.08 ± 0.01 | 0.10 ± 0.01 | 0.10 ± 0.01 | 0.09 ± 0.01 | |
| Ti−Zr | | (3.64) | (3.67) | (3.70) | |
| distance (Å) | | 3.71 ± 0.02 | 3.64 ± 0.02 | 3.77 ± 0.02 | |
| number | | 1.5, fixed | 3, fixed | 4.5, fixed | |
| σ (Å) | | 0.10 ± 0.01 | 0.10 ± 0.01 | 0.10 ± 0.01 | |
| $R^2$ | 1.2284 | 1.4941 | 1.2695 | 1.3576 | |

| | irradiated | | | | |
|---|---|---|---|---|---|
| sample | $y = 0$ | $y = 0.25$ | $y = 0.5$ | $y = 0.75$ | $y = 1.0$ |
| Ti−O$_{48f}$ | | | | | |
| distance (Å) | 1.91 ± 0.02 | 1.92 ± 0.02 | 1.89 ± 0.01 | 1.91 ± 0.01 | |
| number | 3.4 ± 0.8 | 2.8 ± 0.8 | 4.1 ± 1.0 | 3.4 ± 0.8 | |
| σ (Å) | 0.00 ± 0.00 | 0.00 ± 0.00 | 0.00 ± 0.00 | 0.00 ± 0.00 | |
| Ti−O$_{8b}$ | | | | | |
| distance (Å) | 2.04 ± 0.02 | 2.03 ± 0.02 | 2.04 ± 0.02 | 2.03 ± 0.02 | |
| number | 2.4 ± 0.6 | 3.0 ± 1.0 | 3.6 ± 1.0 | 2.6 ± 0.6 | |
| σ (Å) | 0.00 ± 0.00 | 0.01 ± 0.00 | 0.00 ± 0.00 | 0.00 ± 0.00 | |
| Ti−Gd | | | | | |
| distance (Å) | 3.59 ± 0.02 | 3.59 ± 0.02 | 3.65 ± 0.02 | 3.51 ± 0.02 | |
| number | 6.5 ± 1.8 | 6, fixed | 6, fixed | 6, fixed | |
| σ (Å) | 0.11 ± 0.01 | 0.14 ± 0.01 | 0.15 ± 0.01 | 0.13 ± 0.01 | |
| Ti−Ti | | | | | |
| distance (Å) | 3.67 ± 0.02 | 3.68 ± 0.03 | 3.75 ± 0.02 | 3.66 ± 0.02 | |
| number | 5.5 ± 1.6 | 4.5, fixed | 3, fixed | 1.5, fixed | |
| σ (Å) | 0.11 ± 0.01 | 0.14 ± 0.01 | 0.10 ± 0.01 | 0.10 ± 0.01 | |
| Ti−Zr | | | | | |
| distance (Å) | | 3.70 ± 0.03 | 3.66 ± 0.02 | 3.72 ± 0.02 | |
| number | | 1.5, fixed | 3, fixed | 4.5, fixed | |
| σ (Å) | | 0.14 ± 0.02 | 0.10 ± 0.01 | 0.10 ± 0.01 | |
| $R^2$ | 0.8188 | 1.3036 | 1.2741 | 0.7910 | |

[a] Values in parentheses are calculated interatomic distances in Å from XRD determinations of the lattice parameter, $a$, and the X anion positional parameter, $x_{48f}$, given in Table 1. These values were interpolated for the $y = 0.25$ composition.

The analyses of the Ti EXAFS suggest that the Ti−O polyhedra are stable in regard to both composition and ion-beam irradiation. Upon irradiation, the most significant change is the increased disorder in the Ti cation shell, as has been observed in the analysis of Ti K-edge EXAFS in previous radiation-damage studies of complex oxides.[23,25−28] Such observations have been interpreted as a loss of second-nearest-neighbor periodicity because of rotation of the coordination polyhedra about shared corners and edges.[26−27]

The Fourier transforms of the Zr K-edge EXAFS for the Gd$_2$(Ti$_{1-y}$Zr$_y$)$_2$O$_7$ series pyrochlores are shown in Figure 10a and b prior to and following irradiation, respectively. No systematic change in the appearance of the transforms is observed as Zr substitutes for Ti on the B cation site, suggesting a similarity of the B site in pyrochlore and the cation site in defect fluorite structures. The intense peaks at an ∼1.5 Å radial distance correspond to the Zr−O shell, and the second intense peak at a radial distance of ∼3.3 Å corresponds to the cation shell composed of Gd and varying proportions of Zr and Ti

atoms. Upon irradiation, the most significant change is the decrease in intensity of the cation shell (∼3.3 Å) for the $y = 0.5$ and 0.75 compositions. For these same compositions, a minor decrease in the intensity of the Zr−O peak at ∼1.5 Å is also observed upon irradiation.

The results of fits to the Zr K-edge EXAFS are given in Table 6. As was observed for the Ti K-edge EXAFS, two oxygen shells were required to represent the Zr−O EXAFS. The shorter Zr−O distance at ∼2.05 Å is in reasonable agreement with the 2.09 Å Zr−O bond length determined from X-ray diffraction studies of Gd$_2$Zr$_2$O$_7$ in the pyrochlore structure.[42] The longer Zr−O interatomic distance, at ∼2.17 Å, is significantly shorter than the 2.28 Å bond length determined for the Gd$_2$Zr$_2$O$_7$ pyrochlore.[42] The longer Zr−O interatomic distance may correspond to oxygen atoms occupying the vacant 8b site. The occupancy of the nominally vacant 8b site suggests that anion disordering occurs throughout the compositional range. Like Ti−O interatomic distances, neither Zr−O interatomic distance display a systematic dependence on composition. Upon irradia-

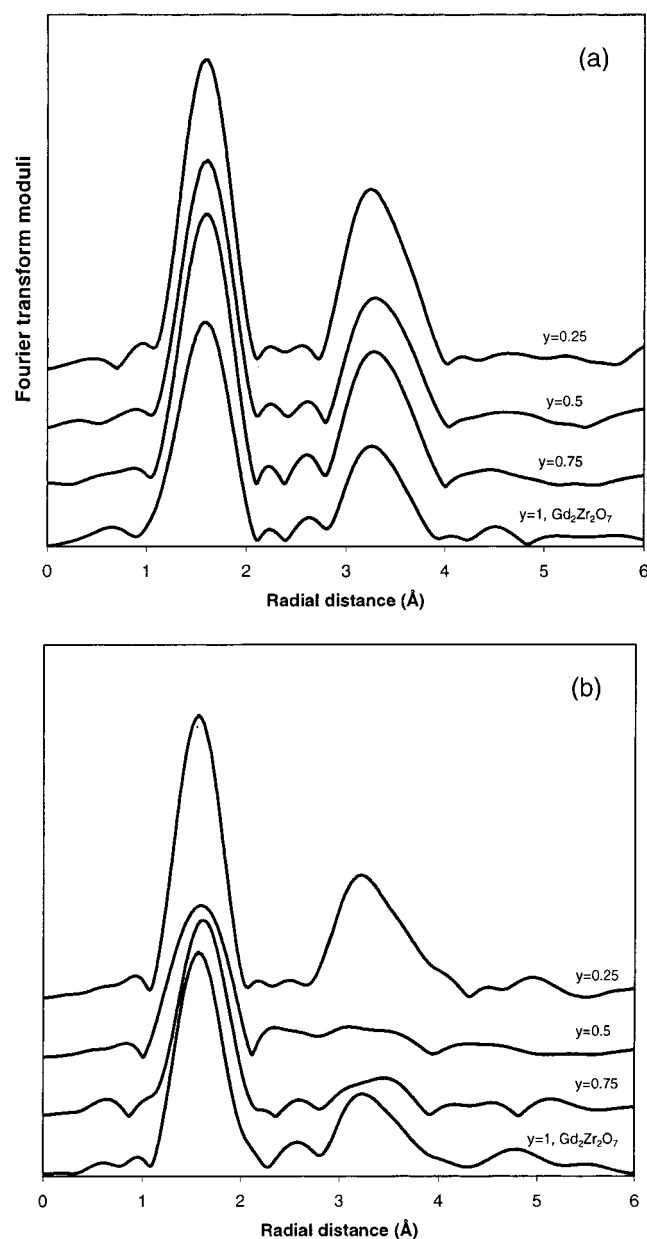**Figure 10.** Fourier transforms of the Zr K-edge EXAFS for the $Gd_2(Zr_yTi_{1-y})_2O_7$ pyrochlore series (a) prior to and (b) following irradiation.

tion, there is a slight increase in both Zr−O interatomic distances for all compositions and a slight decrease in the number of coordinating oxygen atoms for the $y = 0.5$ and 0.75 compositions.

The fitting results for the Zr cation shell suggest that the Zr−Gd and Zr−Zr interatomic distances are similar and increase slightly with increasing Zr substitution. The Zr−Ti interatomic distance is slightly longer than the Zr−Gd and Zr−Zr distances but displays no systematic dependence on composition. The longer Zr−Ti interatomic distance was also suggested by the analysis of the Ti K-edge EXAFS. Upon irradiation, there is an apparent decrease in the Zr−Zr interatomic distance and no change in the Zr−Gd and Zr−Ti interatomic distances. The Zr cation shells for the $y = 0.5$ and 0.75 compositions have significant increases in $\sigma$ that reflect the decreased transform-peak intensity observed at ∼3.3 Å in Figure 10b.

**Discussion**

Our experimental results on the compositionally- and radiation-induced phase transition between pyrochlore and defect

fluorite structures can be considered in terms of the disordering of oxygen atoms on the anion sublattice and the relative stability of the A and B cation sites in the pyrochlore structure. The use of experimental techniques that probe the structures at different length scales affords additional insight into the nature of the phase transition.

Disordering of oxygen atoms on the anion sublattice throughout the compositional series is most apparent in the analysis of the Ti and Zr K-edge EXAFS data and the Raman spectra. The determination of two oxygen bond lengths coordinating Ti and Zr from the EXAFS analysis suggests that oxygen atoms occupy the vacant 8b anion site, which indicates anion disorder across the compositional series. The resulting distribution of oxygen atoms at different bond lengths may also contribute to the unusually broad fwhm of the Raman vibrational modes throughout the compositional series. However, upon irradiation, neither of these experimental techniques indicates significant changes in the degree of anion disorder for a given composition.

Analysis of the EXAFS data also highlights the relative stability of the nearest-neighbor oxygen atoms coordinating the B cation (Ti/Zr) with increasing Zr substitution compared to the nearest-neighbor oxygen atoms coordinating the Gd cation that changes progressively from a pyrochlore-like environment to a fluorite-like environment with increasing Zr substitution. The structural stability of the nearest-neighbor coordination environment of the B cation site relative to that of the Gd cation site is also indicated by the normal-mode analysis of the vibrational data that indicates strong B−O force constants and weak-to-nonexistent Gd−O force constants across the compositional series. EXAFS analysis of the next-nearest-neighbors coordinating the Gd and B cations, which consist of Gd, Ti, and Zr atoms, indicates little or no change as a function of composition, suggesting that both cation environments are structurally stable at this slightly longer length scale. The Raman and infrared spectra display a nearly continuous evolution of spectral features as a function of composition, further supporting the EXAFS results that suggest localized distortion of the cation sites. In particular, the polarized Raman spectra indicate a substantial decrease in the polarizability of the $A_{1g}$ mode at the $y = 0.25$ composition, which indicates a significant change in symmetry at this composition. Note that the XRD results in Table 1 indicate that the pyrochlore structure is retained until the Zr endmember composition is attained. The apparent discrepancy is resolved when one considers that diffraction-based techniques require atomic periodicity over hundreds of angstroms whereas vibrational and XAS spectroscopy reflect atomic structure and symmetry over a few angstroms. Reconciliation of the disparate results suggests that the structural rearrangement of the cation sites occurs locally throughout the compositional series but the overall long-range pyrochlore structure is maintained until the Zr endmember composition is reached.

Following irradiation, EXAFS analysis largely indicates that the nearest-neighbor oxygen atoms coordinating the Gd cation adopt a defect fluorite-like structure whereas the nearest-neighbor oxygen atoms coordinating the B cation (Ti or Zr atoms) exhibit only minor increased displacements. However, the decreased Fourier transform amplitude of the Gd cation shell (∼3.3 Å) indicates that the next-nearest atoms coordinating both Gd and the B cation are significantly disordered for the $y = 0.25$ and 0.75 compositions upon irradiation. Such disorder likely results from rotations about shared polyhedra edges and corners. These conclusions are supported by the infrared vibrational data that show significant changes upon irradiation.

Phase Transition in Gd$_2$(Ti$_{1-y}$Zr$_y$)$_2$O$_7$ Pyrochlores

*J. Phys. Chem. B, Vol. 106, No. 18, 2002* **4675**

**TABLE 6: Zr K-edge EXAFS Fitting Results for the Gd$_2$(Zr$_y$Ti$_{1-y}$)$_2$O$_7$ Pyrochlore Series, Unirradiated**[a]

| sample | y = 0 | y = 0.25 | y = 0.5 | y = 0.75 | y = 1.0 |
|---|---|---|---|---|---|
| Zr−O$_{48f}$ | | (1.97) | (2.00) | (2.05) | (2.09/2.28)[b] |
| distance (Å) | | 2.05 ± 0.01 | 2.05 ± 0.01 | 2.04 ± 0.01 | 2.06 ± 0.01 |
| number | | 3.5 ± 0.7 | 3.0 ± 0.7 | 2.4 ± 0.6 | 2.3 ± 0.6 |
| $\sigma$ (Å) | | 0.00 ± 0.00 | 0.00 ± 0.00 | 0.00 ± 0.00 | 0.080 ± 0.00 |
| Zr−O$_{8b}$ | | | | | |
| distance (Å) | | 2.17 ± 0.01 | 2.17 ± 0.01 | 2.16 ± 0.01 | 2.18 ± 0.01 |
| number | | 2.4 ± 0.6 | 2.7 ± 0.6 | 4.0 ± 0.9 | 3.2 ± 0.6 |
| $\sigma$ (Å) | | 0.00 ± 0.00 | 0.00 ± 0.00 | 0.04 ± 0.02 | 0.05 ± 0.02 |
| Zr−Gd | | (3.64) | (3.67) | (3.70) | (3.72) |
| distance (Å) | | 3.64 ± 0.01 | 3.65 ± 0.02 | 3.66 ± 0.02 | 3.68 ± 0.02 |
| number | | 6, fixed | 6, fixed | 6, fixed | 5.4 ± 1.6 |
| $\sigma$ (Å) | | 0.09 ± 0.01 | 0.09 ± 0.01 | 0.11 ± 0.01 | 0.12 ± 0.01 |
| Zr−Ti | | (3.64) | (3.67) | (3.70) | (3.72) |
| distance (Å) | | 3.70 ± 0.02 | 3.70 ± 0.02 | 3.63 ± 0.02 | |
| number | | 4.5, fixed | 3, fixed | 1.5, fixed | |
| $\sigma$ (Å) | | 0.07 ± 0.01 | 0.10 ± 0.01 | 0.09 ± 0.02 | |
| Zr−Zr | | (3.64) | (3.67) | (3.70) | (3.72) |
| distance (Å) | | 3.61 ± 0.02 | 3.67 ± 0.02 | 3.70 ± 0.02 | 3.69 ± 0.01 |
| number | | 1.5, fixed | 3, fixed | 4.5, fixed | 2.7 ± 0.8 |
| $\sigma$ (Å) | | 0.07 ± 0.01 | 0.10 ± 0.01 | 0.10 ± 0.01 | 0.08 ± 0.01 |
| $R^2$ | | 0.9031 | 0.8616 | 0.9124 | 0.9221 |

| | | | irradiated | | |
|---|---|---|---|---|---|
| sample | y = 0 | y = 0.25 | y = 0.5 | y = 0.75 | y = 1.0 |
| Zr−O$_{48f}$ | | | | | |
| distance (Å) | | 2.06 ± 0.01 | 2.03 ± 0.01 | 2.09 ± 0.01 | 2.09 ± 0.01 |
| number | | 3.7 ± 0.9 | 1.9 ± 0.5 | 2.8 ± 0.7 | 3.4 ± 0.8 |
| $\sigma$ (Å) | | 0.00 ± 0.00 | 0.00 ± 0.00 | 0.00 ± 0.00 | 0.00 ± 0.00 |
| Zr−O$_{8b}$ | | | | | |
| distance (Å) | | 2.20 ± 0.01 | 2.17 ± 0.01 | 2.23 ± 0.02 | 2.24 ± 0.02 |
| number | | 2.6 ± 0.6 | 2.6 ± 0.6 | 2.0 ± 0.5 | 2.5 ± 0.7 |
| $\sigma$ (Å) | | 0.03 ± 0.00 | 0.00 ± 0.00 | 0.00 ± 0.00 | 0.00 ± 0.00 |
| Zr−Gd | | | | | |
| distance (Å) | | 3.64 ± 0.01 | 3.65 ± 0.02 | 3.61 ± 0.02 | 3.65 ± 0.02 |
| number | | 6, fixed | 6, fixed | 6, fixed | 6, fixed |
| $\sigma$ (Å) | | 0.10 ± 0.01 | 0.12 ± 0.01 | 0.12 ± 0.01 | 0.12 ± 0.01 |
| Zr−Ti | | | | | |
| distance (Å) | | 3.72 ± 0.02 | 3.79 ± 0.03 | 3.78 ± 0.02 | |
| number | | 4.5, fixed | 3, fixed | 1.5, fixed | |
| $\sigma$ (Å) | | 0.08 ± 0.01 | 0.11 ± 0.01 | 0.11 ± 0.01 | |
| Zr−Zr | | | | | |
| distance (Å) | | 3.61 ± 0.02 | 3.62 ± 0.02 | 3.62 ± 0.03 | 3.71 ± 0.02 |
| number | | 1.5, fixed | 3, fixed | 4.5, fixed | 6, fixed |
| $\sigma$ (Å) | | 0.08 ± 0.01 | 0.11 ± 0.01 | 0.12 ± 0.01 | 0.11 ± 0.01 |
| $R^2$ | | 1.0418 | 0.8176 | 1.2077 | 0.9663 |

[a] The values in parentheses are calculated interatomic distances in Å from XRD determinations of the lattice parameter, $a$, and the X anion positional parameter, $x_{48f}$, given in Table 1. These values were interpolated for the $y = 0.25$ composition. [b] Based on $x_{48f} = 0.4089$ reported in the literature;[42] however, XRD results indicate that this sample is predominately defect fluorite structured with minor pyrochlore.

For pyrochlore compositions of $0.25 = y = 1.0$, the changes in the infrared spectra are similar upon irradiation, suggesting that a similar defect fluorite structure is adopted in each of these samples at a localized length scale. The XRD patterns of the irradiated pyrochlore samples detected transformation to either an amorphous or defect fluorite structure depending on composition, indicating that the long-range order of the pyrochlore structure is disrupted by radiation damage. Combined, these results indicate that ion-beam irradiation significantly affects the pyrochlore structure primarily along shared polyhedra edges at the second-nearest neighbor or the cation coordination sphere with complete disruption of the crystallinity at the X-ray length scale.

A structural model of the compositionally driven phase transition from the pyrochlore to defect fluorite structure would be dominated by changes in the local Gd environment with little change in the long-range structure. The structural flexibility of the Gd environment is supported by the results of the normal-mode analysis that indicate essentially zero force constants for six of the eight Gd−O bonds, namely, those oxygen atoms at 48f sites. In Figure 11, a ball-and-stick representation of the pyrochlore structure is presented where the thickness of the sticks represents the strength of the linear bond. It is apparent that the pyrochlore structure consists of two interpenetrating but nonconnecting lattices. One consists of Ti and O48f atoms, and the other, of Gd and O8a atoms. The O48f atoms that complete the Gd anion coordination environment are able to accommodate Zr substitution at the B site. A structural model of the radiation-driven phase transition from the pyrochlore to defect fluorite structure, which results in localized changes in the Gd environment and the disorder of the second coordination environment, is formed by rotations along shared TiO$_6$ and GdO$_8$ polyhedral edges and between shared TiO$_6$ polyhedral corners that lead to the disruption of the long-range order observed by XRD.

## Conclusions

Analysis of the spectroscopic results confirms that the structural integrity of the pyrochlore structure can be attributed
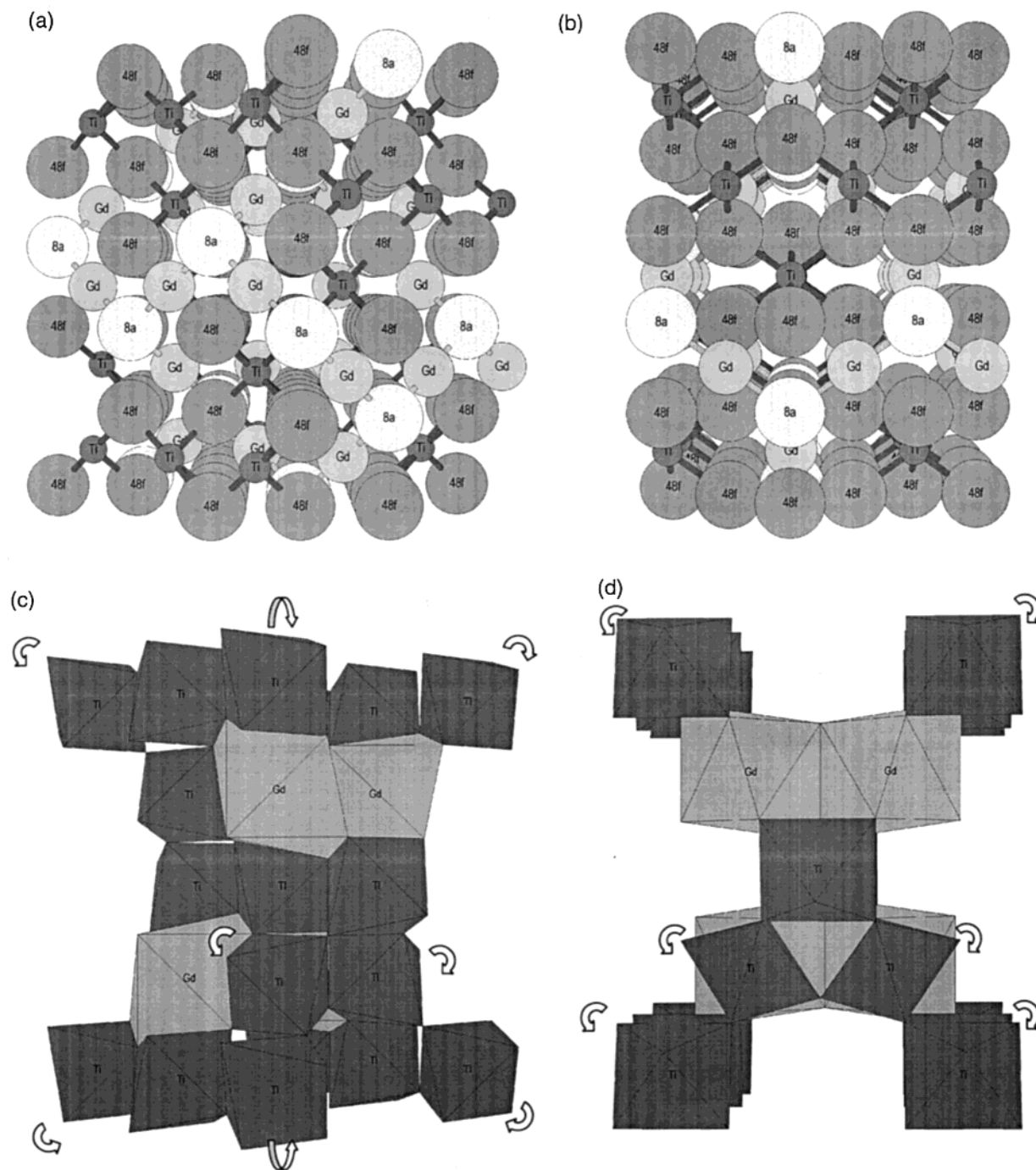
**Figure 11.** Crystallographic models of the $Gd_2Ti_2O_7$ pyrochlore. Ball-and-stick representations of the interpenetrating $TiO_6$ network (dark grays) and $GdO_8$ network (light grays) in the (a) [100] orientation and (b) [110] orientation. Polyhedra representation showing possible rotations of the $TiO_6$ polyhedra about shared corners with other $TiO_6$ polyhedra or shared edges with $GdO_8$ polyhedra in response to ion-beam irradiation for the (c) [100] orientation and the (d) [110] orientation.

to corner-shared distorted $BO_6$ octahedra, as first proposed by Subramanian.[12] Furthermore, for the $Gd_2(Ti_{1-y}Zr_y)_2O_7$ series, the compositionally driven pyrochlore-to-fluorite phase transitions accompanying Zr substitution for Ti involve both anion and cation disorder whereas the radiation-driven phase transition is dominated by cation disorder and interpolyhedral rotations along edges and corners.

Phase Transition in Gd$_2$(Ti$_{1-y}$Zr$_y$)$_2$O$_7$ Pyrochlores

*J. Phys. Chem. B, Vol. 106, No. 18, 2002* **4677**

**Supporting Information Available:** Table 1S lists the comparison of the vibrational force constants calculated using the program VIBRATZ to those observed experimentally. The material is available free of charge via the Internet at http://pubs.acs.org.

## References and Notes

(1) Weber, W. J.; Ewing, R. C.; Catlow, R. C. A.; Diaz de la Rubia, T.; Hobbs, L. W.; Kinoshita, C.; Matzke, Hj.; Motta, A. T.; Nastasi, M.; Salje, E. K. H.; Vance, E. R.; Zinkle, S. J. *J. Mater. Res.* **1998**, *13*, 434.

(2) Weber, W. J.; Ewing, R. C. *Science (Washington, D.C.)* **2000**, *289*, 2051.

(3) Begg, B. D.; Hess, N. J.; Weber, W. J.; Devanathan, R.; Icenhower, J. P.; Thevuthasan, S.; McGrail, B. P. *J. Nucl. Mater.* **2001**, *288*, 208.

(4) Weber, W. J.; Wald, J. W.; Matzke, Hj. *Mater. Lett.* **1985**, *3*, 173.

(5) Weber, W. J.; Wald, J. W.; Matzke, Hj. *J. Nucl. Mater.* **1986**, *138*, 196.

(6) Weber, W. J.; Hess, N. J. *Nucl. Instrum. Methods* **1993**, *B80/81*, 1245.

(7) Lumpkin, G. R.; Ewing, R. C. *Phys. Chem. Miner.* **1988**, *16*, 2.

(8) Wang, S. X.; Begg, B. D.; Wang, L. M.; Ewing, R. C.; Weber, W. J.; Govidan Kutty, K. V. *J. Mater. Res.* **1999**, *14*, 4470.

(9) Wang, S. X.; Wang, L. M.; Ewing, R. C.; Govindan Kutty, K. V. *Mater. Res. Soc. Symp. Proc.* **1999**, *540*, 355.

(10) Begg, B. D.; Hess, N. J.; Weber, W. J.; Conradson, S. D.; Schweiger, M. J.; Ewing, R. C. *J. Nucl. Mater.* **2000**, *278*, 212.

(11) Moon, P. K. Electrical Conductivity and Structural Disorder in Gd$_2$-Ti$_2$O$_7$-Gd$_2$Zr$_2$O$_7$ and Y$_2$Ti$_2$O$_7$-Y$_2$Zr$_2$O$_7$ Solid Solutions. Ph.D. Thesis, Massachusetts Institute of Technology, Cambridge, MA, 1988.

(12) Subramanian, M. A.; Aravamudan, G.; Subba Rao, G. V. *Prog. Solid State Chem.* **1983**, *15*, 55.

(13) Oueslati, M.; Balkanski, M.; Moon, P. K.; Tuller, H. L. *Mater. Res. Soc. Symp. Proc.* **1989**, *135*, 199.

(14) Heremans, C.; Wuensch, B. J.; Stalick, J. K.; Prince, E. *J. Solid State Chem.* **1995**, *117,* 108.

(15) Klee, W. E.; Weitz, G. *J. Inorg.Chem.* **1969**, *31*, 2367.

(16) Scheetz, B. E.; White, W. B. *J. Am. Chem. Soc.* **1979**, *62*, 460.

(17) McCauley, R. A. *J. Opt. Soc. Am.* **1973**, *63*, 721.

(18) McCaffrey, J. F.; McDevitt, N. T.; Phillippi, C. M. *J. Opt. Soc. Am.* **1971**, *61*, 209.

(19) Zhang, M.; Salje, E. K. H.; Farnum, I.; Graeme-Barber, A.; Daniel, P.; Ewing, R. C.; Clark, A. M.; Leroux, H. *J. Phys.: Condens. Matter* **2000**, *12*, 1915.

(20) Zhang, M.; Salje, E. K. H.; Capitani, G. C.; Leroux, H.; Clark, A. M.; Schlüter, H.; Ewing, R. C. *J. Phys.: Condens. Matter* **2000**, *12*, 3131.

(21) Nasdala, L.; Irmer, G.; Wolf, D. *Eur. J. Mineral.* **1995**, *7*, 471.

(22) Nasdala, L.; Pidgeon, R. T.; Wolf, D. *Geochim. Cosmochim. Acta* **1996**, *60*, 1091.

(23) Hawthorne, F. C.; Groat, L. A.; Raudsepp, M.; Spike, F. D.; Gaba, R.; Halden, N. M.; Lumpkin, G. R.; Ewing, R. C.; Greegor, R. B.; Lytle, F. W.; Ercit, T. S.; Rossman, G. R.; Wicks, F. J.; Ramick, R. A.; Sherriff, B. L.; Fleet, M. E.; McCammon, C. *Am. Mineral.* **1991**, *76*, 370.

(24) Weber, W. J.; Hess, N. J.; Maupin, G. D. *Nucl. Instrum. Methods Phys. Res., Sect. B* **1992**, *65*, 102.

(25) Lumpkin, G. R.; Ewing, R. C.; Chakoumakos, B. C.; Greegor, R. B.; Lytle, F. W.; Foltyn, E. M.; Clinnard, F. W., Jr.; Boatner, L. A.; Abraham, M. M. *J. Mater. Res.* **1986**, *1*, 564.

(26) Ewing, R. C.; Chakoumakos, B. C.; Lumpkin, G. R.; Murakami, T.; Greegor, R. B.; Lytle, F. W. *Nucl. Instrum. Methods Phys. Res., Sect. B* **1988**, *32*, 487.

(27) Farges, F.; Ewing, R. C.; Brown, G. E., Jr. *J. Mater. Res.* **1993**, *8*, 1983.

(28) Greegor, R. B.; Lytle, F. W.; Livak, R. J.; Clinnard, F. W., Jr. *J. Nucl. Mater.* **1988**, *152*, 270.

(29) Hess, N. J.; Weber, W. J.; Conradson, S. D. *J. Nucl. Mater.* **1998**, *254*, 175.

(30) Thevuthasan, S.; Peden, C. H. F.; Engelhard, M. H.; Baer, D. R.; Herman, G. S.; Jiang, Y.; Weber, W. J. *Nucl. Instrum. Methods Phys. Res., Sect. A* **1999**, *420*, 81.

(31) Begg, B. D.; Hess, N. J.; McCready, D. E.; Thevuthasan, S.; Weber, W. J. *J. Nucl. Mater.* **2001**, *289*, 188.

(32) Knop, O.; Brisse, F.; Castelliz, L. *Can. J. Chem.* **1969**, *47*, 971.

(33) Vandenborre, N. T.; Husson E.; Brusset, H. *Spectrochim. Acta, Part A* **1981**, *32*, 113.

(34) Dowty, E. *VIBRAT,* version 1.1; SHAPE SOFTWARE: 1999; www.shapesoftware.com.

(35) Ankudinov, A. L.; Conradson, S. D.; Mustre de Leon, J.; Rehr, J. J. *Phys. Rev. B: Condens. Matter* **1998**, *57*, 7518.

(36) Ankudinov, A. L.; Ravel, B.; Rehr, J. J.; Conradson, S. D. *Phys. Rev. B: Condens. Matter* **1998**, *58*, 7565.

(37) Rehr, J. J.; Ankudinov, A.; Zabinsky, S. I. *Catal. Today* **1998**, *39*, 263.

(38) Mustre de Leon, J.; Conradson, S. D.; Clark, D. L.; Denauwer, C.; Hess, N. J.; Keogh, D. W. *J. Am. Chem. Soc.*, submitted for publication, 2001.

(39) McMaster, W. H.; Kerr del Grande, N.; Mallett, J. H.; Hubbell, J. H. *Compilation of X-ray Cross Sections*; University of California: Livermore, CA, 1969.

(40) Ankudinov, A. L. Self-energy models in XAFS, XANES and XMCD. Ph.D. Thesis, University of Washington, Seattle, WA, 1996.

(41) Rehr, J. J.; Mustre de Leon, J.; Zabinsky S. I.; Albers, R. C. *J. Am. Chem. Soc.* **1991**, *113*, 5135.

(42) Moriga, T.; Yoshiasa, A.; Kanamaru, F.; Koto, K.; Yoshimura, M.; Somiya, S. *Solid State Ionics* **1989**, *31*, 319.

(43) Mihailova, B.; Stoyanov, S.; Gaydarov, V.; Gospodinov, M.; Konstantinov, L. *Solid State Commun.* **1997**, *103*, 623.

(44) Peters, G. G.; Hayes, J. M.; Hieftje, G. M. *Chemical Separations and Measurements: Theory and Practice of Analytical Chemistry*; W. B. Saunders: Philadelphia, 1974; Chapter 18.

(45) Chtoun, E.; Hanebali, L.; Garnier, P.; Kiat, J. M. *Eur. J. Solid State Inorg. Chem.* **1997**, *34*, 553.

(46) Haile, S. M.; Wuensch, B. J.; Prince, E. *Mater. Res. Soc. Symp. Proc.* **1990**, *166*, 81.

(47) Becker, W. J.; Will, G. *Z. Kristallogr.* **1970**, *131*, 278.

(48) Becker, W. J.; Will, G. *Z. Naturforsch.* **1969**, *24*, 259.